Long-lived Ag₁₀6+ luminescence and a split DNA scaffold

Cite as: J. Chem. Phys. 154, 244302 (2021); doi: 10.1063/5.0056214

Submitted: 7 May 2021 • Accepted: 10 June 2021 •

Published Online: 23 June 2021







Jeffrey T. Petty, Description Savannah Carnahan, Dahye Kim, and David Lewis

AFFILIATIONS

Department of Chemistry, Furman University, Greenville, South Carolina 29613, USA

Note: This paper is part of the JCP Special Topic on From Atom-Precise Nanoclusters to Superatom Materials.

a) Author to whom correspondence should be addressed: jeff.petty@furman.edu

ABSTRACT

Molecular silver clusters emit across the visible to near-infrared, and specific chromophores can be formed using DNA strands. We study C₄AC₄TC₃G that selectively coordinates and encapsulates Ag₁₀⁶⁺, and this chromophore has two distinct electronic transitions. The green emission is strong and prompt with $\phi = 18\%$ and $\tau = 1.25$ ns, and the near-infrared luminescence is weaker, slower with $\tau = 50 \,\mu s$, and is partly quenched by oxygen, suggesting phosphorescence. This lifetime can be modulated by the DNA host, and we consider two derivatives of C₄AC₄TC₃G with similar sequences but distinct structures. In one variant, thymine was excised to create an abasic gap in an otherwise intact strand. In the other, the covalent phosphate linkage was removed to split the DNA scaffold into two fragments. In relation to the contiguous strands, the broken template speeds the luminescence decay by twofold, and this difference may be due to greater DNA flexibility. These modifications suggest that a DNA can be structurally tuned to modulate metastable electronic states in its silver cluster

Published under an exclusive license by AIP Publishing. https://doi.org/10.1063/5.0056214

I. INTRODUCTION

When metals shrink from their bulk to nanoscale forms, the continuous bands of delocalized molecular orbitals segregate, and these distinct electronic states yield novel features.¹⁻⁴ For example, while bulk silver is distinguished by its high broadband reflectivity, Snm-sized silver nanoclusters and clusters develop diverse and distinct colors with strong absorption and emission across the visible to near-infrared.^{5–7} These metallic chromophores become viable labels and sensors when they can be sequestered from their environment and synthesized with specific spectra and brightness, as illustrated by silver-based cellular labels and analyte sensors.^{8,9} This protection and tunability are realized with ligands that coordinate and stabilize metallic clusters and electronically tune the cluster spectra and brightness. 4,9,10 DNA ligands for emissive silver clusters are considered in these studies.

Single-stranded DNAs are polymeric ligands whose nucleobases collectively encapsulate few-atom silver molecules, and the DNA length, sequence, and structure program the cluster spectra and brightness. 11-14 Strands with 10-30 nucleobases prescribe cluster stoichiometry by coordinating and concentrating a limited

number of Ag+, which are chemically reduced and then coalesce to form metal-like clusters. 15-17 Specific sequences further regulate the cluster size and spectra because the four canonical nucleobases have different affinities for silver. 18,19 Additionally, distinct DNA structures form because oligonucleotides are flexible and can fold and assemble around their cluster adducts, and these structures, in turn, regulate cluster brightness.^{20–22} To illustrate, single-stranded DNA-silver cluster conjugates unfold and hybridize with complementary strands, and the reorganized DNA boosts cluster emission by over 10³-fold.^{23,24} In these studies, the DNA structure is controlled by dividing a strand into two fragments that together bind the

DNA-bound silver clusters are bright because their emissive and ground states are efficiently coupled, as evidenced by extinction coefficients ~10⁵ M⁻¹ cm⁻¹, fluorescence quantum yields (QYs) reaching ~0.9, and ns-lived emission. 18,26,27 However, their emission can be perturbed by metastable, lower-lying dark states, which are powerful tools for fluorescence imaging and sensing.^{28–32} Characterizing such states will advance our understanding of the moleculelike electronic structure in silver nanoclusters, and we identified such a state in C₄AC₄TC₃G:Ag₁₀⁶⁺. ³³ We chose this oligonucleotide

because it has the minimal length and specific sequence to preferentially form a Ag₁₀⁶⁺ adduct. This strand is organized into the three tracts: C₄A, C₄T, and C₃G, from which removing or altering a single nucleobase disrupts the cluster binding site. These tracts assemble into a folded structure, and we studied the junction at thymine. The Ag_{10}^{6+} adduct yields strong green fluorescence, but the emissive state is partly quenched by a neighboring state that is nominally dark. However, shifting our spectral window reveals longlived, near-infrared luminescence whose lifetime decreases when the phosphate backbone of C₄AC₄TC₃G is broken at the thymine junction. This observation suggests that the structure of a DNA host can control metastable states in its silver cluster adducts.

II. EXPERIMENTAL

A. Synthesis

The DNA-bound silver clusters were synthesized in a typical bottom-up approach.³⁴ Three desalted, single-stranded oligonucleotides (Integrated DNA Technologies) were used: C4AC4TC3G, C₄AC₄T, and C₃GT. These were dissolved in deionized water, and the DNA concentrations were determined using extinction coefficients derived from the nearest-neighbor approximation.³⁵ These DNA strands were combined with Ag⁺ at a 1:8 relative ratio at a DNA concentration of 30 µM in either water or a 5 mM cacodylic acid/cacodylate buffer at pH = 7. This relative concentration limited the number of species.³⁶ Next, an aqueous solution of BH₄⁻ was added to give a final concentration of 4 BH₄-:oligonucleotide. After mixing, the samples were then placed in a high-pressure reactor from Parr with 400 psi O2 for ~3 h. These reaction conditions preferentially favor the Åg₁₀⁶⁺ cluster over alternate species.³

B. Excision

Uracil-DNA Glycosylase (UDG) was used because it can costeffectively modify a diverse range of DNA sequences.^{22,37} It was obtained from New England BioLabs (M0280S) and stored at −20 °C. The DNA strand C₄AC₄UC₃G, where U is uracil, was modified by using 15 μ l of 1 mM of the DNA solution, 7.5 μ l of enzyme (3.5 units), and 5 μ l of 10× reaction buffer [from the supplier but without dithiothreitol (DTT)] in a total volume of 50 μ l. Slow pipetting mixed the solution to preserve the enzyme activity. The resulting solution was incubated at 37 °C for ~1 h and subsequently dialyzed against water. The extinction coefficient for this strand accounted for the excised nucleobase.

C. Data collection

Absorption spectra were collected on a Cary 50 UV-Vis spectrophotometer (Varian), and steady state emission spectra were collected on a Fluoromax-3 spectrofluorometer (Jobin-Yvon Horiba). Fluorescence quantum yields (QYs) were measured using fluorescein at pH = 10 as the standard (QY = 95%).38 Mass spectra were collected using a Q-TOF G2-S (Waters) in the negative ionization mode and analyzed with MassLynx V4.1. 17,39-41 Time-correlated single photon counting used a pulsed 470 nm laser (PicoQuant) at a pulse repetition rate of 10 MHz. The excitation beam was vertically polarized, and its power was adjusted to achieve a detection rate of fewer than five photons per 100 pulses ($<5 \times 105$ Hz). The emission was collected at a right angle with the emission polarizer set to the magic angle (~55°) and spectrally filtered using a 565/20 nm filter. The instrument response function (IRF) was collected using colloidal silica (Aldrich), and its FWHM was ~150 ps. The kinetics of fluorescence decay was extracted through IRF convolution fitting of the measured decay (FluoFit).

The longer-lived luminescence was collected by using a modulated laser. The argon ion laser was operated at 496 nm, and neutral density filters were used to control its intensity. An acoustooptic modulator with a fixed frequency driver (MT200-A0.5-VIS, AA Opto-Electronic) modulated the laser intensity. The fixed frequency driver was supplied with a square waveform with a peakto-peak amplitude of 0-1 V from a function generator (33250A, Agilent). The laser was focused by a 10× objective (rms10×, Thorlabs) to a spot with a 3.5 μm radius inside a 3 \times 3 mm fluorescence cell (3.3-45-Q-3, Starna Cells). The fluorescence was collected at 90° through either the 565/20 filter for the green emission or 737LP/842SP filters for the near-infrared emission and detected by using an avalanche photodiode (APD) (SPD-050, Micro Photon Devices). The transistor-transistor logic (TTL) pulses from the detector were processed by using a counter/timer card (PCI-6612, National Instruments), operated in the multichannel scaling mode. The card was triggered by using the function generator and histogrammed the clock ticks (100 MHz) between consecutive APD pulses. The samples were thermostatted using a water bath. The absorbance of the solutions was ~ 0.05 .

The off time of the laser controls the excited state populations and relaxation. Diffusion is slow on the ~200 μ s time scale of the modulated laser excitation (see Fig. 2) because the DNA-silver cluster diffusion coefficient is $140 \, \mu \text{m}^2/\text{s}$ and the focused laser beam has diameter ~4 μ m. ^{22,42} Relatively low irradiances limit photobleaching and photoconversion, as supported by matching rates for the fluorescence decay and luminescence growth.

For Stern-Volmer analysis, samples were purged for 4 min and then capped. Lifetimes (τ) were fit using

$$\frac{\tau_0}{\tau}=1+k_q\tau_0[O_2],$$

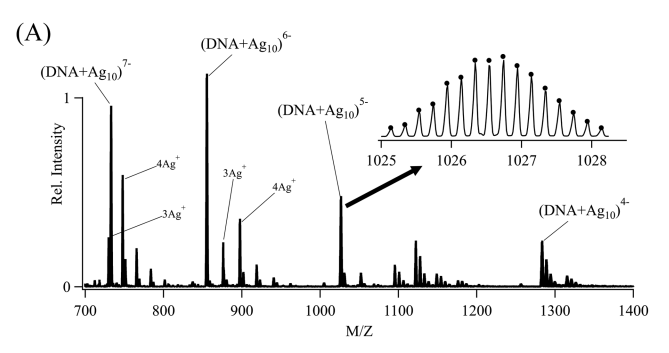
where τ_0 is the lifetime with nitrogen purging, k_q is the quenching constant, and [O2] is the concentration of O2. The oxygen concentration was calculated from Henry's law constant of 1.2×10^{-5} $mol/(Pa m^3).^{43}$

The state populations from the Jablonski diagram were modeled using Mathematica 12.1.0 (see Appendix I).

III. RESULTS

A. Partially reduced, fluorescent Ag₁₀⁶⁺ adduct

The C₄AC₄TC₃G oligonucleotide favors a specific silver molecule whose stoichiometry and charge were measured by electrospray ionization mass spectrometry. The DNA controls the ionization of these complexes through its phosphates, which become partially neutralized with labile H⁺ during desolvation. 41,44 $C_4AC_4TC_3G$ forms ions with -7, -6, -5, and -4 overall charges due to incremental numbers of phosphate-bound H⁺, and each ion has ten bound silvers [Fig. 1(a)]. These likely coalesce to form



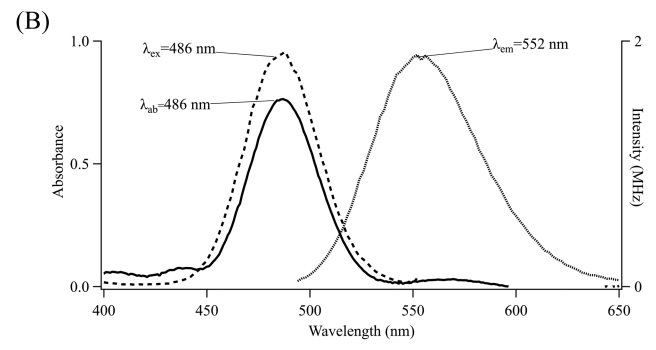


FIG. 1. (a) Mass:charge spectrum of the -7, -6, -5, and -4 charged ions of $C_4AC_4TC_3G-Ag_{10}^{6+}$. Minor peaks are due to three and four Ag^+ adducts with $C_4AC_4TC_3G$ (Fig. S3). (Inset) Isotopologue distribution for (DNA- Ag_{10}^{6+}) $^{-5}$ is reproduced by $C_{129}H_{159}N_{45}O_{82}P_{13}Ag_{10}$ with a precision of 0.8 ± 0.3 ppm (black dots). (b) Absorption (left) and excitation/emission (right) spectra of $C_4AC_4TC_3G-Ag_{10}^{6+}$. Overlapping absorption/excitation bands support a single DNA-cluster chromophore. The minor absorption peak at \sim 570 nm is attributed to another silver cluster (Fig. S7).

clusters with metal-like bonds based on x-ray spectroscopy studies of other DNA-Ag₁₀⁶⁺ complexes.^{39,40} In addition to becoming heavier, C₄AC₄TC₃G is partially neutralized by its Ag₁₀ adduct, as revealed through the number of labile H⁺.27,45 These hydrogens leave because the cluster is partly oxidized, and the displaced hydrogens were counted by using the isotope fine structure in the mass spectra, as illustrated by -5 charged C₄AC₄TC₃G without and with Ag₁₀ [Fig. 1(a) (inset) and Figs. S1 and S2]. The naturally occurring isotopes yield distinct isotopologues whose distributions are atomically sensitive to single hydrogen precision. The free strand shows a sparse set of peaks because C, H, N, O, and P have dominant isotopes, and the positions and intensities of these peaks are faithfully replicated by the formula $C_{129}H_{165}N_{45}O_{32}P_{13}^{5-}$ (Fig. S1A, left). The fine structure for corresponding C₄AC₄TC₃G:Ag₁₀ is denser because the added silvers have two isotopes in equivalent proportions: 51.8% ¹⁰⁷Ag and 48.2% ¹⁰⁹Ag (Fig. S1A, right). This peak envelope was reproduced by the formula $C_{129}H_{159}N_{45}O_{32}P_{13}Ag_{10}^{5-}$. The underlined H's emphasize that the latter complex has six fewer H⁺ than the native strand yet maintains its overall -5 charge. These observations suggest that six H⁺ are displaced from the DNA because six of the 10 bound silvers are oxidized, i.e., Ag₁₀⁶⁺. The same analysis for the -4, -6, and -7 states again support the Ag_{10}^{6+} adduct (Fig. S2). The confidence in this oxidation state is bolstered by the measurement precision, as shifts by $\pm 1~\text{H}^+$, giving less reliable predictions (Fig. S1B). We highlight that DNA-bound ${\rm Ag_{10}}^{6+}$ has been studied both in gas phase using mass spectrometry and in solution using x-ray spectroscopy, and both approaches yield matching oxidation states. 40 We finally note that $\rm C_4AC_4TC_3G$ also binds 3 and 4 $\rm Ag^+$, but these fully oxidized adducts are not expected to be visible chromophores (Fig. S3). 16

The C₄AC₄TC₃G scaffold was biochemically and chemically modified to yield two new templates with similar sequences but distinct structures. We targeted the thymine because prior studies of the related C₄AC₄TC₃GT₄ showed that the oligonucleotide folds at the interior thymine junction.^{22,25} Additionally, thymine is a poor ligand, and other studies directly and indirectly show that it does not interact with silver clusters. 19,46-48 Thus, modifying this site is not expected to directly perturb the $Ag_{10}^{\ 6+}$ coordination site and emission. In one variant, the thymine was selectively removed from the DNA polymer-it was first replaced with a uracil, which was then specifically excised with Uracil-DNA glycosylase (Fig. S4).^{37,49} The mass spectra show that the resulting C₄AC₄XC₃G now has an abasic site X with an intact deoxyribose-phosphodiester backbone but still forms the ${\rm Ag_{10}}^{6+}$ adduct. In another variant, the backbone was broken at the thymine to produce two fragments (Fig. S5). We used C₄AC₄T and C₃GT because the latter strand is commercially available and the added thymine is an innocuous nucleobase.²⁵ These fragments mimic the contiguous C₄AC₄TC₃G and reassemble as a bifurcated scaffold without covalently linking 5'-phosphate to again form Ag₁₀⁶⁺. 11,15,50</sup>

With these DNA scaffolds, Ag_{10}^{6+} is the only molecularly sized, partially reduced adduct in the mass spectra and, thus, is like the chromophore in the optical spectra [Fig. 1(b)]. With $C_4AC_4TC_3G$, the Ag_{10}^{6+} chromophore absorbs at 486 nm and emits at 552 nm, and it is the only chromophore in the spectra [Fig. 1(b) and Fig. S6].⁵¹ Ag_{10}^{6+} is favored because mild oxidizing conditions eliminate alternate species.³⁶ This DNA-cluster complex is a strong fluorophore with an amplitude-weighted lifetime of 1.25 \pm 0.03 ns and a fluorescence quantum yield of 18% \pm 2%.^{52,53} The modified strands yield similar chromophores, which suggests that the similar sequences yield the same binding sites (Table 1). However, the DNA structural differences are imprinted on slower fluorescence and luminescence changes of the Ag_{10}^{6+} adduct.

B. Diminished and slow fluorescence

The emission from C₄AC₄TC₃G:Ag₁₀⁶⁺ is strong but tempered when using a laser. The fluorescence increases linearly at lower

TABLE I. Spectroscopic and photophysical constants for the ${\rm Ag_{10}}^{6+}$ clusters with the three DNA templates. $^{\circ}$

Oligonucleotide	$\lambda_{ab}/\lambda_{em} (nm)^b$	$\tau_{\rm f}({\rm ns})^{\rm c}$	$\varphi_f\left(\%\right)^d$	$\tau_{\rm L} (\mu s)^{\rm e}$
$C_4AC_4TC_3G$	486/552	1.25 ± 0.03	18 ± 2	53 ± 3
$C_4AC_4XC_3G$	486/553	1.28 ± 0.01	20 ± 1	53 ± 3
$C_4AC_4T + C_3GT$	488/553	1.55 ± 0.04	21 ± 3	26 ± 1

^aAll measurements collected at 20 °C.

 $[^]b Absorption \, (\lambda_{ab})$ and emission (λ_{em}) maxima.

^cGreen fluorescence lifetimes.

^dGreen fluorescence quantum yields.

^eNear-infrared luminescence lifetimes.

irradiances and continues to increase but sublinearly at \$50 W/cm², which corresponds to an excitation rate of ~10 kHz based on an extinction coefficient of ~50 000 $M^{-1}~cm^{-1}$ (Fig. S8). This rate falls well below the ~800 MHz emission rate, so excitation-emission cycling is not saturated. We consider an intermediate state that lies below and thereby depletes the emissive state, as identified for other DNA-bound silver clusters through fluorescence blinking, lifetime, and intensity measurements [Fig. 2(a)]. $^{56-62}$ In our studies, this neighboring state is investigated through fluorescence-based kinetic studies.

A kinetic model shows how an intermediate state can indirectly limit fluorescence.⁶³ The energy diagram is based on the three states S₀ (ground), S₁ (emissive), and D/State 2 (luminescent) with rate constants that are derived from earlier and our

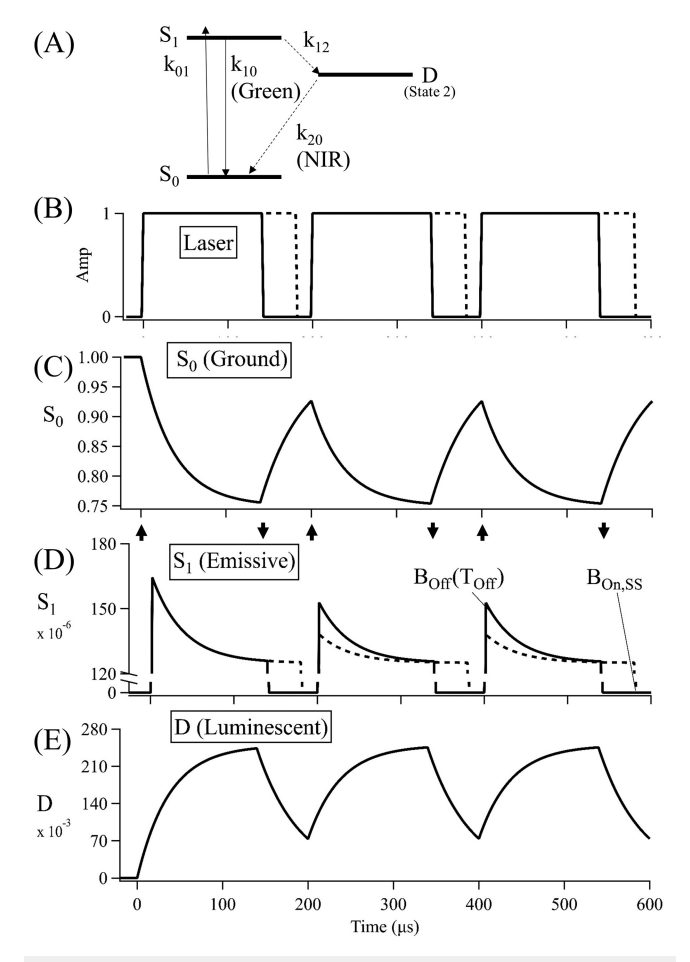


FIG. 2. (a) Electronic model for $C_4AC_4TC_3G-Ag_{10}^{6+}$ with ground (S_0) , emissive (S_1) , and intermediate (D) states and with connecting rate constants. The dashed lines emphasize relatively slow transitions to and from D. (b) Three laser excitation cycles at 5 kHz with $T_{OFF}=60$ (solid) and 10 (dotted) μs . [(c)–(e)] Time evolution of the relative populations in S_0 , S_1 , and D, respectively. The small arrows indicate when the laser is on and off. The S_1 population is shown with the $T_{OFF}=60$ (solid) and 10 (dotted) μs excitations from (b). Both reach the same steady state intensity ($B_{ON,SS}$), but the 140 μs cycle has a higher initial intensity [$B_{OFF}(T_{OFF})$] because it recovers to a greater extent between cycles. Note the break in the ordinate for (d) that emphasizes the limited dynamic range of the fluorescence decay.

present studies [Fig. 2(a)]. 54,57,61,63 In prior studies, the D state has been fluorescently dark, but we subsequently show that this state in C₄AC₄TC₃G:Ag₁₀⁶⁺ yields near-infrared luminescence. The $S_0 \rightarrow S_1$ excitation rate constant is $k_{01} = \sigma I$, and our typical irradiance (I) of 300 W/cm² and an absorption cross section (σ) of 2 × 10⁻¹⁶ cm²/mol (ϵ = 50 000 M⁻¹ cm⁻¹) give k_{01} = 140 kHz.^{24,25} This irradiance exceeds the ~10 kHz threshold that tempers the fluorescence; thus, population is driven to the D state (Fig. S8). The $S_1 \rightarrow S_0$ relaxation rate constant $k_{10} = 800$ MHz is derived from the 1.25 ns fluorescence lifetime (Table I). The $D \rightarrow S_0$ relaxation rate $k_{20} = 20$ kHz, which was derived from the decay of the green emission and near-infrared luminescence from this cluster [Figs. 3(a) and 4(b)]. The crossing rate constant $k_{12} = \phi_{12}k_{10} = 40$ MHz was calculated from the ϕ_{12} = 5% quantum yield for $S_1 \rightarrow D$ in the present studies, consistent with prior results (Fig. S10).^{56,57} Thermally activated reverse crossing from $D \rightarrow S_1$ may not be significant because we do not observe delayed fluorescence. 64 The differential rate equations that connect these states yield the time-dependent state populations, which are experimentally controlled by modulating the laser intensity in an on/off, square wave manner [see Appendix I and compare Fig. 2(b) with Figs. 2(c)-2(e)]. ^{63,65} When the laser is on, the DNA-clusters should be rapidly driven from S₀ to S₁ but then gradually accumulate in D to yield a steady state S₀-S₁-D distribution. When the laser is then turned off, the excited clusters should return to the ground state—rapidly from S₁ and gradually from D. However, if the laser is turned back on too soon, this recovery would be interrupted, and the steady state distribution would be re-established [dotted lines in Figs. 2(b) and 2(d)]. We discuss two sets of kinetic studies—first of green emission from S1 and then of near-infrared luminescence from D.

The disparity in the rate constants for the S_1 and D states simplifies the kinetic model for our data (see Appendix II), 65

$$B \stackrel{k_{\text{ON}}}{\rightleftharpoons} D. \tag{1}$$

A collective bright state B is used because the emissive S_1 state is strongly coupled with the ground S_0 state via laser excitation and prompts ~ns emission. Thus, populations in these two states equilibrate, and their aggregate population is monitored via the green emission. This bright state weakly couples with and is drained by its lower-lying D neighbor through the rate constants k_{ON} and k_{OFF} , which are $\phi_{12}k_{10}$ and k_{20} , respectively, in the three-level model [Fig. 2(a)]. 66 k_{ON} and k_{OFF} are derived from the following analytical rate equations that describe the fluorescence intensity as the laser is modulated. When the laser is on, the bright state population (BoN) is initially high and then exponentially decays,

$$B_{ON}(t) = \frac{k_{OFF}}{k_{ON} + k_{OFF}} + \frac{k_{ON}}{k_{ON} + k_{OFF}} e^{-(k_{ON} + k_{OFF})t}.$$
 (2)

After the laser is on for an extended period, a steady state population B_{ON,SS} is achieved,

$$B_{ON,SS} = \frac{k_{OFF}}{k_{ON} + k_{OFF}}. (3)$$

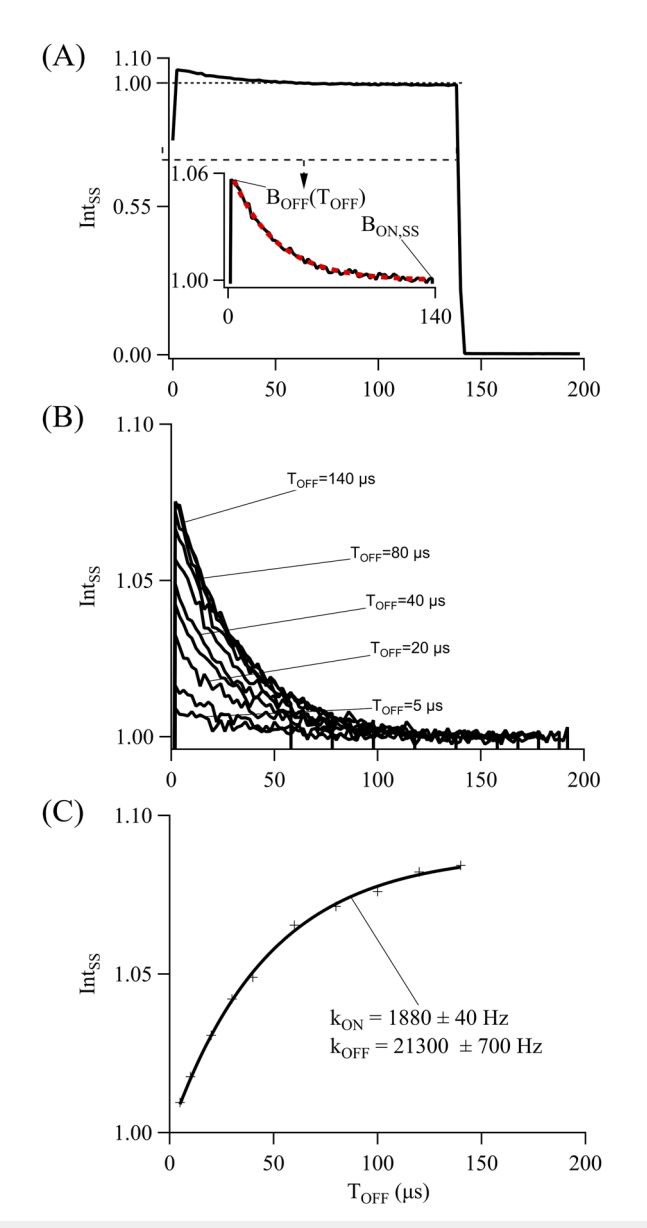
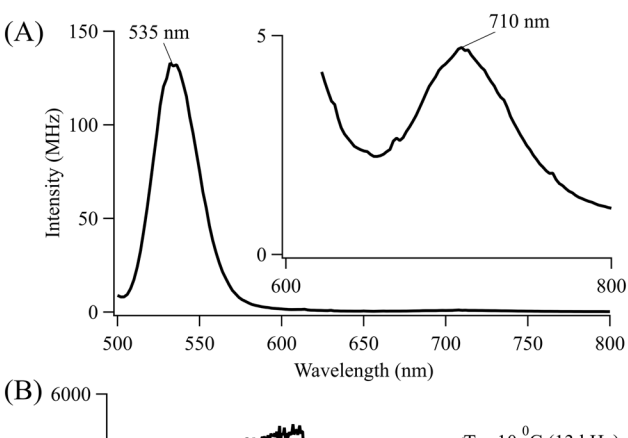


FIG. 3. (a) Green fluorescence decay when $C_4AC_4TC_3G-Ag_{10}^{6+}$ is excited at 496 nm at 5 kHz with 60/140 μ s off/on times. (Inset) Fluorescence decay when the laser is on. An exponential fit (red) determined the amplitude $[B_{OFF}(T_{OFF})]$ and baseline $(B_{ON,SS})$. The dynamic range of the decay is limited because the bright state population is large and only slightly perturbed by D. (b) A series of fluorescence decays with different off times (T_{OFF}) . The amplitudes are suppressed with shorter off times. The decays have similar rates (within a 10% range) and reach the same steady state intensity. (c) Normalized intensities from the above panel were fit with Eq. (5) to determine K_{ON} and K_{OFF} .

When the laser is turned off, the steady state bright state population (B_{OFF}) is initially low but is replenished as the excited clusters exit the long-lived D state, 65

$$B_{OFF}(T_{OFF}) = 1 - \frac{k_{ON}}{k_{ON} + k_{OFF}} e^{-k_{OFF}T_{OFF}}.$$
 (4)



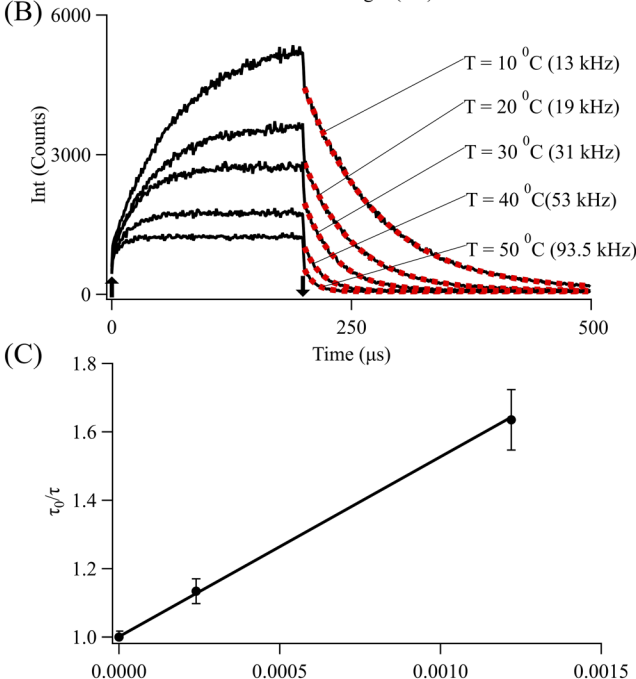


FIG. 4. (a) Fluorescence spectra collected with $\lambda_{ex}=490$ nm in an ethylene glycol–aqueous glass at 77 K. Both strong green fluorescence ($\lambda=535$ nm) and near-infrared luminescence (see inset— $\lambda=710$ nm) are produced. (b) Time evolution of the near-infrared luminescence using a 1 kHz modulated laser with a 200 μ s on time. A single exponential fit (red) during the off period for the laser yielded a $k_{OFF}=19.6\pm0.1$ kHz. Up and down arrows indicate when the laser is on and off. (c) Stern–Volmer plot derived from the near-infrared luminescence lifetimes without (τ_0) and with (τ) oxygen ([O₂]). The slope $\tau_0 k_{SV}$ from the linear fit yielded $k_{SV}=9~(\pm1)\times10^6~M^{-1}~s^{-1}$.

 $[O_2](M)$

 $T_{\rm OFF}$ is the time the laser is off, and longer $T_{\rm OFF}$ increases the bright state population and hence fluorescence. This recovered population was normalized using the steady state population,

$$Int_{SS} = \frac{B_{OFF}(T_{OFF})}{B_{ON,SS}} = 1 + \frac{k_{ON}}{k_{OFF}} \left(1 - e^{-k_{OFF}T_{OFF}}\right).$$
 (5)

The predicted fluorescence decay and recovery in Fig. 2(d) are observed for $C_4AC_4TC_3G:Ag_{10}^{6+}$. The laser was modulated at 5 kHz at an irradiance of 300 W/cm², and the fluorescence kinetics were

controlled by manipulating T_{OFF} from 5 to 140 μs during the 200 μs laser period [Figs. 3(a) and 3(b)]. These fluorescence decays settle to the same steady state intensity, but their initial amplitudes are bolstered with longer off times. These decays were adequately fit with single exponentials, and the resulting amplitudes and baselines were used to determine $B_{OFF}(T_{OFF})$ and $B_{ON,SS}$, respectively [see labels in Fig. 3(a)]. The ratio $B_{OFF}(T_{OFF})/B_{ON,SS}$ was then plotted vs the off times and fit using Eq. (5). The resulting $k_{OFF} = 22 \pm 3$ kHz at 20 °C was also obtained at different modulation frequencies and laser intensities (Fig. S9). k_{ON} was also derived from the fit, and it was used to calculate the crossing efficiency ϕ_{12} in the three-level model [Fig. 2(a)],

$$k_{ON} = k_{01}\phi_{12} = \sigma I\phi_{12}.$$
 (6)

The linear dependence of k_{ON} with the irradiance gives $\phi_{12}=5\%\pm1\%$ from the slope, with $\sigma=8\times10^{-17}$ cm2/mol (Fig. S10).²⁵ As a reference, Eosin Y was also studied because it has an intermediate triplet state that is analogous to the D state for $C_4AC_4TC_3G:Ag_{10}^{6+}$. This variation of k_{ON} with the laser irradiance gives $\phi_{12}=55\%$, consistent with previous studies.⁶⁷

C. Near-infrared luminescence

The green fluorescence decay and recovery indirectly support a nominally dark D state that quenches emission [Figs. 2(a) and 3]. However, a possible spectroscopic signature for this state is observed in a cryogenic aqueous/ethylene glycol glass. The DNA-cluster chromophore still not only has strong green emission, shifted to 535 nm, but also has weaker luminescence at 710 nm [Fig. 4(a)]. At room temperature, this near-infrared luminescence is still observed but is kinetically sluggish in relation to the green emission [compare Figs. 3(a) and 4(b)]. When the laser is on, the green fluorescence promptly jumps to its maximum before settling to its elevated steady state intensity, whereas the near-infrared signal slowly grows to a plateau. When the laser is turned off, the fluorescence abruptly ceases, while the near-infrared luminescence slowly decays. This slow near-infrared growth and decay are mirrored by our kinetic model in which D is inefficiently populated through the higher-lying S_1 and then slowly relaxes back to S_0 [compare Figs. 4(b) and 2(e)]. We propose that the near-infrared luminescence is a direct signature of the D state via a D \rightarrow S₀ radiative relaxation. An exponential decay of this signal is predicted by our simplified kinetic scheme [Eq. (1)], so exponential fits during the off time of the laser yielded k_{OFF} (see Appendix II),

$$D_{OFF}(t) = \frac{k_{ON}}{k_{ON} + k_{OFF}} e^{-k_{OFF}t}.$$
 (7)

This $k_{OFF} = 19 \pm 1$ kHz matches $k_{OFF} = 22 \pm 3$ kHz derived from the fluorescence measurements, which suggests that only the S_1 and D states are coupled [Fig. 4(b)]. Single exponential fits adequately describe these decays, which support a single type of cluster, as also supported by the fluorescence spectra [Fig. 1(b) and Fig. S6]. The rates are consistent over a 20-fold variation in the DNA concentration, which indicates that dilute solutions avoid self-quenching (Fig. S11).

Relaxation from D is $\sim 10^4 \times$ slower than the $S_1 \rightarrow S_0$ decay, and the quantum yield ϕ_{12} for entering D is only 5%. These inefficiencies suggest that passing to and from D may be spin-forbidden, so the electron organization of this state was probed with

oxygen as a paramagnetic quencher. Solutions were saturated with nitrogen, air, and oxygen at ambient pressure, and the luminescence decays faster with O₂ [Fig. 4(c)]. Stern–Volmer analysis supports dynamic quenching because lifetime and intensity ratios match. The resulting dynamic quenching constant of 9 (±1) × 10⁶ M⁻¹ s⁻¹ is significantly lower than a theoretical value based on the diffusion coefficients of 2 × 10⁻⁵ cm²/s and 1.4 × 10⁻⁶ cm²/s for O₂ and the DNA-Ag₁₀⁶⁺ complex, respectively, and a collisional radius of 10 Å. 22,69,70 The relatively lower observed rate constant supports a cluster that is embedded within a DNA matrix.

The near-infrared luminescence also decays faster at higher temperatures [Fig. 4(b) and Fig. S12]. The decay rates increase ~7 fold from 13 to 94 kHz from 10 to 50 °C. These changes are reversible and may signify that the cluster is robust but able to adapt to the structure of its DNA host. 23,24,47,60 Similar effects of temperature have been noted for phosphorescent chromophores in proteins and peptides. 71 The two structural variants of $C_4AC_4XC_3G$ and $C_4AC_4T+C_3GT$ were also studied. Both form $Ag_{10}^{\ 6+}$ adducts with strong green emission and weaker near-infrared luminescence such as the parent strand (Figs. S4 and S5 and Table I). While the abasic $C_4AC_4XC_3G$ mimics its parent with similar near-infrared decays, the split $C_4AC_4T+C_3GT$ scaffold yields a $Ag_{10}^{\ 6+}$ that decays twofold faster at 20 °C, and this difference holds over a wide temperature range (Table I and Table S1). This suggests that the broken backbone destabilizes the D state.

IV. DISCUSSION

The phosphate backbone of DNA is a structural roadmap for DNA-silver cluster complexes. It prescribes the number and sequence of nucleobases that directly coordinate the cluster, and it folds around to encapsulate its cluster adduct. Collectively, a binding pocket for a specific silver cluster develops. In these studies, we targeted the backbone in C₄AC₄TC₃G:Ag₁₀⁶⁺ at its folded thymine junction. One derivative eliminated the thymine while preserving the phosphate linkage and the other severed the phosphate linkage to create a bifurcated scaffold. Both mimic their parent strand by producing $Ag_{10}^{\ 6+}$ with strong, prompt green emission, so they preserve the nucleobases that directly coordinate the cluster. Beyond the immediate coordination site, the peripheral backbone changes are signaled by the near-infrared luminescence from these complexes, which decays twofold faster in the split vs the contiguous strands. This enhanced D \rightarrow S₀ relaxation may stem from the breached backbone and hence greater flexibility in the split scaffold. DNA strands fluctuate over multiple time scales, so slow conformational changes may be coupled with these long-lived electronic states. 60,72 To systematically explore this relationship, the DNA flexibility could be synthetically tuned by rejoining the $C_4AC_4T + C_3GT$ fragments via ethylene glycols. These linkers are more flexible than the canonical phosphodiester backbone, and their length can be varied to kinetically map changes in DNA structure and flexibility.⁷³ Other two-stranded DNA scaffolds might be similarly modified. $^{74-77}$

A fundamental function of DNA is to encapsulate and protect its cluster adduct. The protective $C_4AC_4TC_3G$ shell around $Ag_{10}^{\ 6+}$ was probed with oxygen, which can penetrate the densely charged DNA matrix because it is uncharged, small, and weakly hydrophilic with limited water solubility.⁷⁸ Furthermore, it is a versatile probe because its triplet ground state collisionally quenches luminescence

from a wide range of chromophores.⁵¹ However, the observed quenching of the metastable C₄AC₄TC₃G:Ag₁₀⁶⁺ complexes is inefficient in relation to diffusional encounters, as also observed with proteins. The phosphorescence from buried tryptophans is prolonged because their reaction with quenchers is hindered.⁷⁹ The Ag₁₀⁶⁺ may be similarly sequestered, as it is coordinated by the nucleobases inside the folded and compact C₄AC₄TC₃G host.^{22,25} Additionally, the chromophore may be a more deeply buried inside a DNA-Ag⁺ shell, as supported EXAFS studies.⁴⁰ In support of such a hierarchal structure, DNA-Ag⁺ shells can be extended by lengthening the DNA without perturbing the reduced cluster chromophore.³⁷ Analogous studies with longer C₄AC₄TC₃G sequences may provide an avenue to modulate the reactivity of the metastable D state.

The near-infrared luminescence from C₄AC₄TC₃G:Ag₁₀⁶⁺ has hallmarks of phosphorescence—it is prominent in cryogenic glasses that limit nonradiative relaxation and quenching, has an ~50 000fold longer lifetime than the green fluorescence, and is quenched with oxygen.⁶⁶ Additionally, D is more electronically stable than S_1 but is inefficiently populated via the optically excited S_1 state. Passage to and from D may be slow because it is spin-forbidden.⁶⁶ Triplet states for small hydrated silver clusters Ag₄(H₂O)₂²⁺ and Ag₄(H₂O)₄²⁺ in zeolites have been identified through theoretical and spectroscopic studies.⁸⁰ Their multiexponential luminescence relaxes over a 0.5-100 µs time span, and this 200-fold range is attributed to the ligand fields of their waters. The luminescence from $C_4AC_4TC_3G:Ag_{10}^{\ 6+}$ has a similarly long decay time but is distinct because it is monexponential and remains as such from 10 to 50 °C with different DNA scaffolds. This suggests that the cluster lies in a homogeneous binding site within the DNA host. This binding site could be modified to alter $S_1 \rightarrow D$ coupling, and we will integrate halogens.⁶⁶ For example, brominating guanosine does not affect the green fluorescence from $Ag_{10}^{\ 6+}$, but this nucleobase may be removed from the binding site.²² We are now studying the halogenation of other nucleobases in C₄AC₄TC₃G.

V. CONCLUSION

DNA strands are versatile platforms that can be synthetically modified through chemical and biochemical means. They are also templates for molecular silver clusters with diverse spectra and brightnesses. These two concepts are combined in these studies and show that the metastable near-infrared luminescence from C4AC4TC3G-Ag $_{10}^{6+}$ depends on the continuity of the phosphodiester backbone. These metastable states could be tuned by synthetically modifying the DNA with the goal of further developing this new class of DNA-bound silver cluster labels and reporters.

SUPPLEMENTARY MATERIAL

See the supplementary material for Figs. S1–S12, Table S1, and Appendixes I and II.

ACKNOWLEDGMENTS

We thank the National Science Foundation (Grants No. CHE-1611451 and 2002910) and the Furman Advantage program.

This work was supported, in part, by the National Science Foundation EPSCoR Program under NSF Award No. OIA-1655740.

DATA AVAILABILITY

The data that support the findings of this study are available within the article and its supplementary material.

REFERENCES

- ¹R. Kubo, J. Phys. Soc. Jpn. **17**(6), 975–986 (1962).
- ²J. Zheng, P. R. Nicovich, and R. M. Dickson, Annu. Rev. Phys. Chem. 58, 409 (2007).
- ³K. L. D. M. Weerawardene, H. Häkkinen, and C. M. Aikens, Annu. Rev. Phys. Chem. **69**(1), 205–229 (2018).
- ⁴K. R. Krishnadas, G. Natarajan, A. Baksi, A. Ghosh, E. Khatun, and T. Pradeep, Langmuir **35**(35), 11243–11254 (2019).
- ⁵I. Rabin, W. Schulze, and G. Ertl, Chem. Phys. Lett. **312**(5–6), 394–398 (1999).
- ⁶L. Gell, A. Kulesza, J. Petersen, M. I. S. Röhr, R. Mitrić, and V. Bonačić-Koutecký, J. Phys. Chem. C 117(28), 14824–14831 (2013).
- ⁷C. P. Joshi, M. S. Bootharaju, and O. M. Bakr, J. Phys. Chem. Lett. **6**(15), 3023–3035 (2015).
- ⁸J. Yu, S. A. Patel, and R. M. Dickson, Angew. Chem., Int. Ed. 46(12), 2028 (2007).
- ⁹X. Kang and M. Zhu, Chem. Soc. Rev. **48**(8), 2422–2457 (2019).
- ¹⁰R. Jin, Nanoscale 7(5), 1549–1565 (2015).
- ¹¹ J. T. Petty, J. Zheng, N. V. Hud, and R. M. Dickson, J. Am. Chem. Soc. **126**(16), 5207–5212 (2004).
- 12 J. M. Obliosca, C. Liu, R. A. Batson, M. C. Babin, J. H. Werner, and H.-C. Yeh, Biosensors 3, 185–200 (2013).
- ¹³ E. Gwinn, D. Schultz, S. Copp, and S. Swasey, Nanomaterials 5(1), 180–207 (2015).
- ¹⁴J. T. Petty, S. P. Story, J.-C. Hsiang, and R. M. Dickson, J. Phys. Chem. Lett. 4(7), 1148–1155 (2013).
- $^{15}\mathrm{M}.$ Daune, C. A. Dekker, and H. K. Schachman, Biopolymers 4, 51–76 (1966).
- ¹⁶T. Yamane and N. Davidson, Biochim. Biophys. Acta 55, 609–621 (1962).
- ¹⁷J. T. Petty, O. O. Sergev, A. G. Kantor, I. J. Rankine, M. Ganguly, F. D. David, S. K. Wheeler, and J. F. Wheeler, Anal. Chem. 87(10), 5302–5309 (2015).
- ¹⁸C. I. Richards, S. Choi, J.-C. Hsiang, Y. Antoku, T. Vosch, A. Bongiorno, Y.-L. Tzeng, and R. M. Dickson, J. Am. Chem. Soc. **130**(15), 5038–5039 (2008).
- ¹⁹S. M. Copp, P. Bogdanov, M. Debord, A. Singh, and E. Gwinn, Adv. Mater. 26(33), 5839–5845 (2014).
- ²⁰D. Schultz, R. G. Brinson, N. Sari, J. A. Fagan, C. Bergonzo, N. J. Lin, and J. P. Dunkers, Soft Matter 15(21), 4284–4293 (2019).
- ²¹ J. T. Petty, B. Giri, I. C. Miller, D. A. Nicholson, O. O. Sergev, T. M. Banks, and S. P. Story, Anal. Chem. 85(4), 2183–2190 (2013).
- ²²J. T. Petty, M. Ganguly, A. I. Yunus, C. He, P. M. Goodwin, Y.-H. Lu, and R. M. Dickson, J. Phys. Chem. C 122(49), 28382–28392 (2018).
- ²³ H.-C. Yeh, J. Sharma, J. J. Han, J. S. Martinez, and J. H. Werner, Nano Lett. 10(8), 3106–3110 (2010).
- ²⁴J. T. Petty, O. O. Sergev, D. A. Nicholson, P. M. Goodwin, B. Giri, and D. R. McMullan, Anal. Chem. 85(20), 9868–9876 (2013).
- ²⁵C. He, P. M. Goodwin, A. I. Yunus, R. M. Dickson, and J. T. Petty, J. Phys. Chem. C **123**(28), 17588–17597 (2019).
- ²⁶J. Sharma, R. C. Rocha, M. L. Phipps, H.-C. Yeh, K. A. Balatsky, D. M. Vu, A. P. Shreve, J. H. Werner, and J. S. Martinez, Nanoscale 4(14), 4107–4110 (2012).
- ²⁷D. Schultz, K. Gardner, S. S. R. Oemrawsingh, N. Markešević, K. Olsson, M. Debord, D. Bouwmeester, and E. Gwinn, Adv. Mater. 25, 2797–2803 (2013).
- ²⁸B. Huang, M. Bates, and X. Zhuang, Annu. Rev. Biochem. 78(1), 993–1016
- ²⁹T. Ha and P. Tinnefeld, Annu. Rev. Phys. Chem. **63**(1), 595–617 (2012).
- ³⁰G. Patterson, M. Davidson, S. Manley, and J. Lippincott-Schwartz, Annu. Rev. Phys. Chem. 61(1), 345–367 (2010).

- ³¹ J.-C. Hsiang, A. E. Jablonski, and R. M. Dickson, Acc. Chem. Res. 47(5), 1545–1554 (2014).
- ³² J. Widengren, J. R. Soc., Interface 7(49), 1135–1144 (2010).
- ³³O. M. Bakr, V. Amendola, C. M. Aikens, W. Wenseleers, R. Li, L. Dal Negro, G. C. Schatz, and F. Stellacci, Angew. Chem., Int. Ed. 48(32), 5921–5926 (2009).
- ³⁴Y.-P. Xie, Y.-L. Shen, G.-X. Duan, J. Han, L.-P. Zhang, and X. Lu, Mater. Chem. Front. 4(8), 2205–2222 (2020).
- ³⁵V. A. Bloomfield, D. M. Crothers, and I. Tinoco Jr., *Nucleic Acids: Structures, Properties, and Functions* (University Science Books, Sausaltio, CA, 2000).
- ³⁶ J. T. Petty, S. P. Story, S. Juarez, S. S. Votto, A. G. Herbst, N. N. Degtyareva, and B. Sengupta, Anal. Chem. **84**(1), 356–364 (2012).
- ³⁷J. T. Petty, M. Ganguly, I. J. Rankine, E. J. Baucum, M. J. Gillan, L. E. Eddy, J. C. Léon, and J. Müller, J. Phys. Chem. C 122(8), 4670–4680 (2018).
- ³⁸ A. M. Brouwer, Pure Appl. Chem. **83**(12), 2213 (2011).
- ³⁹J. T. Petty, M. Ganguly, I. J. Rankine, D. M. Chevrier, and P. Zhang, J. Phys. Chem. C 121(27), 14936–14945 (2017).
- ⁴⁰ J. T. Petty, O. O. Sergev, M. Ganguly, I. J. Rankine, D. M. Chevrier, and P. Zhang, J. Am. Chem. Soc. 138(10), 3469–3477 (2016).
- ⁴¹N. Potier, A. Van Dorsselaer, Y. Cordier, O. Roch, and R. Bischoff, Nucleic Acids Res. 22(19), 3895–3903 (1994).
- ⁴²T. Spielmann, H. Blom, M. Geissbuehler, T. Lasser, and J. Widengren, J. Phys. Chem. B **114**(11), 4035–4046 (2010).
- ⁴³ R. Sander, Atmos. Chem. Phys. **15**(8), 4399–4981 (2015).
- ⁴⁴R. H. Griffey, H. Sasmor, and M. J. Greig, J. Am. Soc. Mass Spectrom. **8**(2), 155–160 (1997).
- 45 K. Koszinowski and K. Ballweg, Chem. Eur. J. 16(11), 3285–3290 (2010).
- ⁴⁶B. Sengupta, C. M. Ritchie, J. G. Buckman, K. R. Johnsen, P. M. Goodwin, and J. T. Petty, J. Phys. Chem. C 112(48), 18776–18782 (2008).
- ⁴⁷ M. Ganguly, C. Bradsher, P. Goodwin, and J. T. Petty, J. Phys. Chem. C 119(49), 27829–27837 (2015).
- ⁴⁸C. Cerretani, J. Kondo, and T. Vosch, CrystEngComm **22**(46), 8136–8141 (2020).
- ⁴⁹N. Schormann, R. Ricciardi, and D. Chattopadhyay, Protein Sci. 23(12), 1667–1685 (2014).
- ⁵⁰R. H. Jensen and N. Davidson, Biopolymers **4**(1), 17–32 (1966).
- $^{51}\mathrm{J.}$ R. Lakowicz, Principles of Fluorescence Spectroscopy, 3rd ed. (Springer, New York, 2006).
- 52 J. R. Lakowicz, Principles of Fluorescence Spectroscopy (Plenum Press, New York, 1999).
- ⁵³ A. Sillen and Y. Engelborghs, Photochem. Photobiol. **67**(5), 475–486 (1998).
- ⁵⁴ W.-T. Yip, D. Hu, J. Yu, D. A. Vanden Bout, and P. F. Barbara, J. Phys. Chem. A 102(39), 7564–7575 (1998).
- 55 T. Basché, W. E. Moerner, M. Orrit, and H. Talon, Phys. Rev. Lett. 69(10), 1516–1519 (1992).

- ⁵⁶I. L. Volkov, P. Y. Serdobintsev, and A. I. Kononov, J. Phys. Chem. C 117(45), 24079–24083 (2013).
- ⁵⁷S. A. Patel, M. Cozzuol, J. M. Hales, C. I. Richards, M. Sartin, J.-C. Hsiang, T. Vosch, J. W. Perry, and R. M. Dickson, J. Phys. Chem. C 113(47), 20264–20270 (2009).
- ⁵⁸J. T. Petty, C. Fan, S. P. Story, B. Sengupta, M. Sartin, J.-C. Hsiang, J. W. Perry, and R. M. Dickson, J. Phys. Chem. B **115**(24), 7996–8003 (2011).
- ⁵⁹ J. T. Petty, C. Fan, S. P. Story, B. Sengupta, A. St. John Iyer, Z. Prudowsky, and R. M. Dickson, J. Phys. Chem. Lett. 1(17), 2524–2529 (2010).
- ⁶⁰C. Cerretani, M. R. Carro-Temboury, S. Krause, S. A. Bogh, and T. Vosch, Chem. Commun. **53**(93), 12556–12559 (2017).
- 61 S. Krause, M. R. Carro-Temboury, C. Cerretani, and T. Vosch, Chem. Commun. 54(36), 4569–4572 (2018).
- ⁶²T. Vosch, Y. Antoku, J.-C. Hsiang, C. I. Richards, J. I. Gonzalez, and R. M. Dickson, Proc. Natl. Acad. Sci. U. S. A. 104(31), 12616–12621 (2007).
- ⁶³T. Sandén, G. Persson, P. Thyberg, H. Blom, and J. Widengren, Anal. Chem. 79(9), 3330–3341 (2007).
- 64 C. A. Parker and C. G. Hatchard, Trans. Faraday Soc. 57, 1894–1904 (1961).
- ⁶⁵D. P. Mahoney, E. A. Owens, C. Fan, J.-C. Hsiang, M. M. Henary, and R. M. Dickson, J. Phys. Chem. B 119(13), 4637–4643 (2015).
- ⁶⁶N. J. Turro, V. Ramamurthy, and J. C. Scaiano, *Modern Molecular Photochemistry of Organic Molecules* (Science Books, 2010).
- ⁶⁷ A. Penzkofer, A. Beidoun, and M. Daiber, J. Lumin. **51**(6), 297–314 (1992).
- ⁶⁸ J. M. Beechem and L. Brand, Annu. Rev. Biochem. **54**(1), 43–71 (1985).
- ⁶⁹S. Doose, H. Barsch, and M. Sauer, Biophys. J. **93**(4), 1224–1234 (2007).
- ⁷⁰D. A. Johnson and J. Yguerabide, Biophys. J. **48**(6), 949–955 (1985).
- ⁷¹M. Gonnelli and G. B. Strambini, Photochem. Photobiol. **81**(3), 614–622 (2005)
- ⁷²D. Andreatta, J. L. Pérez Lustres, S. A. Kovalenko, N. P. Ernsting, C. J. Murphy, R. S. Coleman, and M. A. Berg, J. Am. Chem. Soc. **127**(20), 7270–7271 (2005).
- 73 W. Pils and R. Micura, Nucleic Acids Res. 28(9), 1859–1863 (2000).
- ⁷⁴D. Schultz and E. G. Gwinn, Chem. Commun. **48**(46), 5748–5750 (2012).
- ⁷⁵J. T. Petty, D. A. Nicholson, O. O. Sergev, and S. K. Graham, Anal. Chem. 86(18), 9220–9228 (2014).
- ⁷⁶C. Cerretani, H. Kanazawa, T. Vosch, and J. Kondo, Angew. Chem., Int. Ed. 58, 17153 (2019).
- ⁷⁷D. J. E. Huard, A. Demissie, D. Kim, D. Lewis, R. M. Dickson, J. T. Petty, and R. L. Lieberman, J. Am. Chem. Soc. **141**(29), 11465–11470 (2019).
- ⁷⁸J. R. Lakowicz and G. Weber, Biochemistry **12**(21), 4161–4170 (1973).
- ⁷⁹P. Cioni and G. B. Strambini, Biochim. Biophys. Acta, Protein Struct. Mol. Enzymol. 1595(1), 116–130 (2002).
- ⁸⁰ D. Grandjean, E. Coutiño-Gonzalez, N. T. Cuong, E. Fron, W. Baekelant, S. Aghakhani, P. Schlexer, F. D'Acapito, D. Banerjee, M. B. J. Roeffaers, M. T. Nguyen, J. Hofkens, and P. Lievens, Science 361(6403), 686–690 (2018).

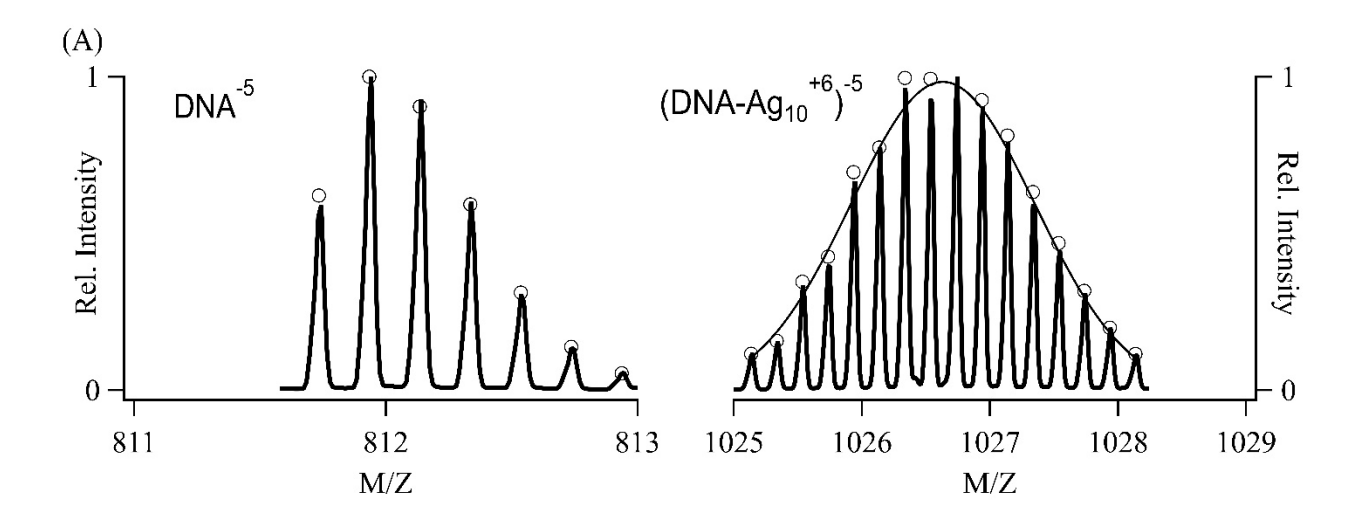
Supplementary Material:

Long-Lived Ag₁₀⁶⁺ Luminescence and a Split DNA Scaffold

Jeffrey T. Petty*, Savannah Carnahan, Dahye Kim, and David Lewis§

§Department of Chemistry, Furman University, Greenville, SC 29163, United States

^{*}corresponding author. Email: <u>jeff.petty@furman.edu</u>



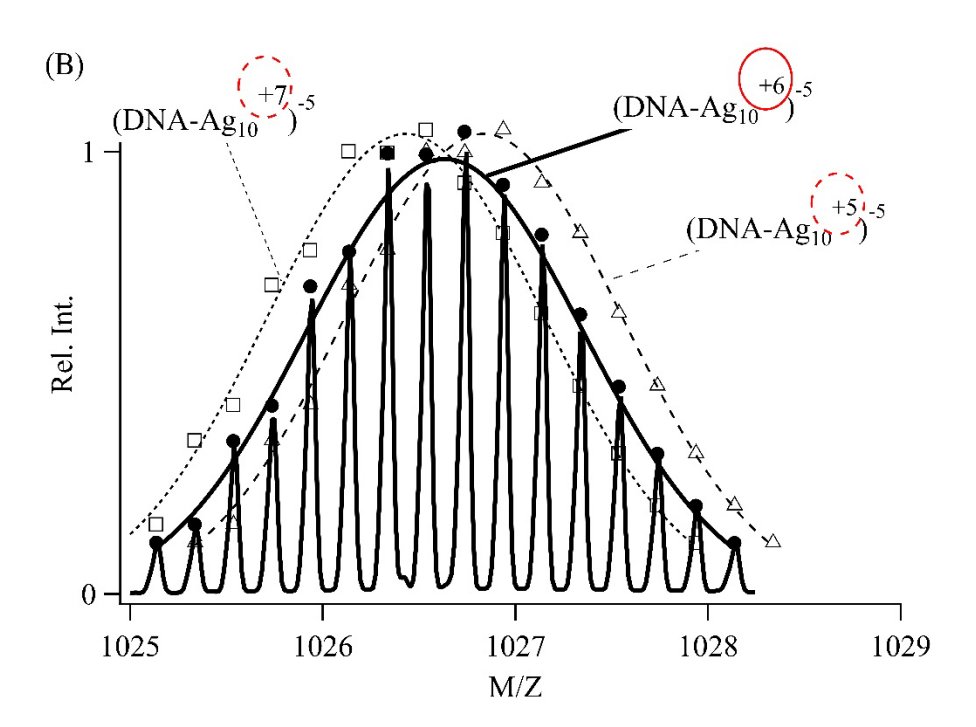


Figure S1: (A) Mass:charge spectrum of the -5 charge states of $C_4AC_4TC_3G$ (left) and $C_4AC_4TC_3G$ - Ag_{10}^{6+} (right). The open circles predict the M/Z values based on the formulas $C_{129}H_{\underline{165}}N_{45}O_{32}P_{13}^{5-}$ and $C_{129}H_{\underline{159}}N_{45}O_{32}P_{13}$ Ag_{10}^{5-} , respectively. The hydrogens are underlined to emphasize that the oxidized Ag_{10}^{6+} displaces 6 H⁺ from the phosphates. The spectrum of (DNA- Ag_{10}^{6+})-5 includes a Gaussian fit to demonstrate the statistical distribution of isotopologues. (B) M/Z spectrum of the -5 charged ion of $C_4AC_4TC_3G$ - Ag_{10}^{6+} . The distributions are predicted using the formulas $C_{129}H_{\underline{159}}N_{45}O_{32}P_{13}$ Ag_{10}^{6+} (filled dots with solid line fit), $C_{129}H_{\underline{160}}N_{45}O_{32}P_{13}$ Ag_{10}^{5+} (open triangles with dashed line fit), and $C_{129}H_{\underline{159}}N_{45}O_{32}P_{13}$ Ag_{10}^{5+} (open squares with dotted line fit). The hydrogens are underlined and the cluster oxidation states are circled to emphasize that a Ag^+ displaces a H⁺. Gaussian fits emphasize that the spectrum with $C_{129}H_{\underline{159}}N_{45}O_{32}P_{13}$ Ag_{10}^{6+} agrees best with the observed envelop of peaks (solid red circle).

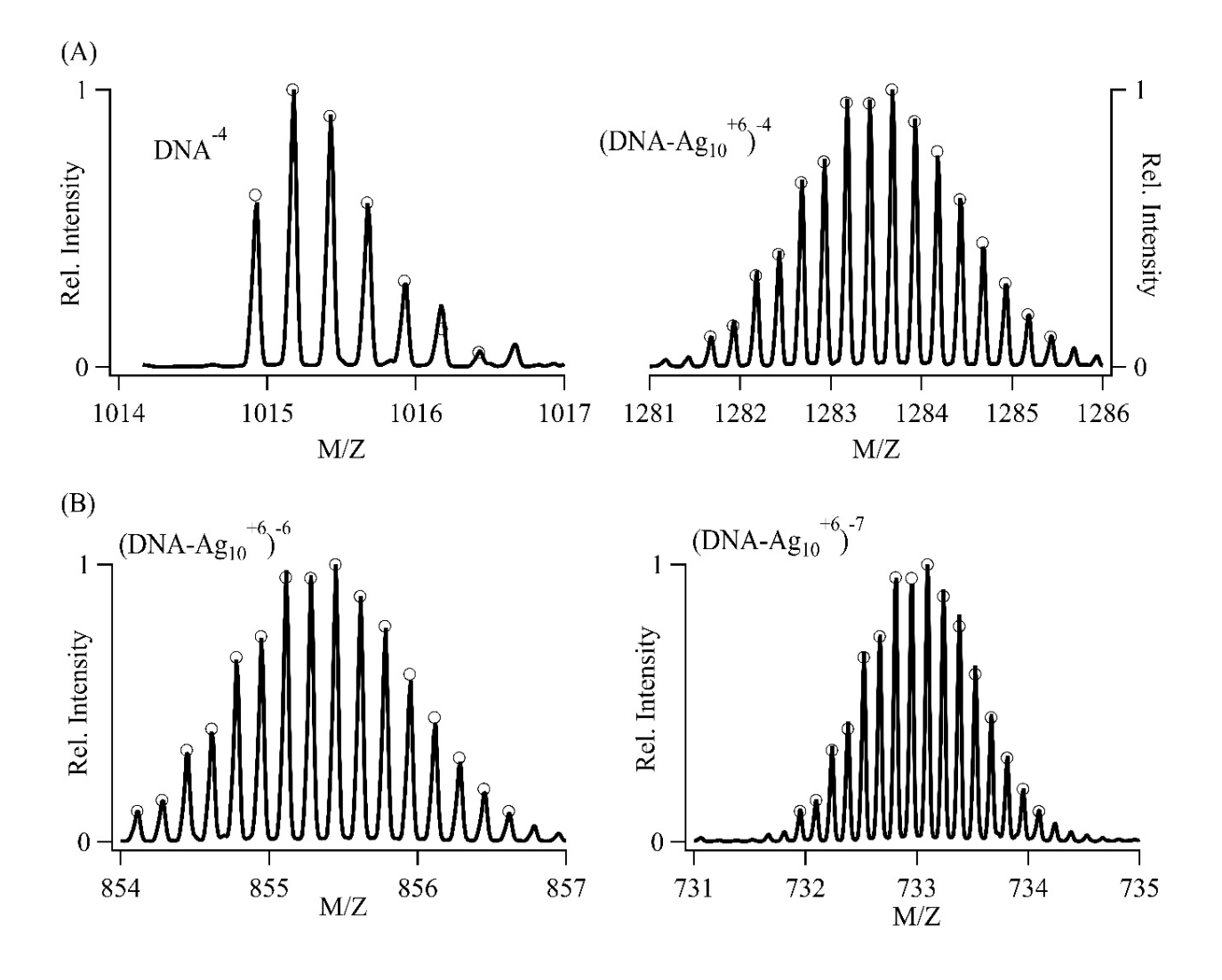


Figure S2: (A) Mass:charge spectrum of the -4 charge states of $C_4AC_4TC_3G$ (left) and $C_4AC_4TC_3G$ - Ag_{10}^{6+} (right). The open circles predict the M/Z values based on the formulas $C_{129}H_{\underline{166}}N_{45}O_{32}P_{13}^{4-}$ and $C_{129}H_{\underline{160}}N_{45}O_{32}P_{13}$ Ag_{10}^{4-} , respectively. The hydrogens are underlined to emphasize that the oxidized Ag_{10}^{6+} displaces 6 H⁺ from the phosphates. (B) Mass:charge spectrum of the -6 and -7 charge states of $C_4AC_4TC_3G_4$ Ag_{10}^{6+} . The open circles predict the M/Z values based on the respective formulas $C_{129}H_{\underline{158}}N_{45}O_{32}P_{13}$ Ag_{10}^{6-} and $C_{129}H_{\underline{157}}N_{45}O_{32}P_{13}$ Ag_{10}^{7-} .

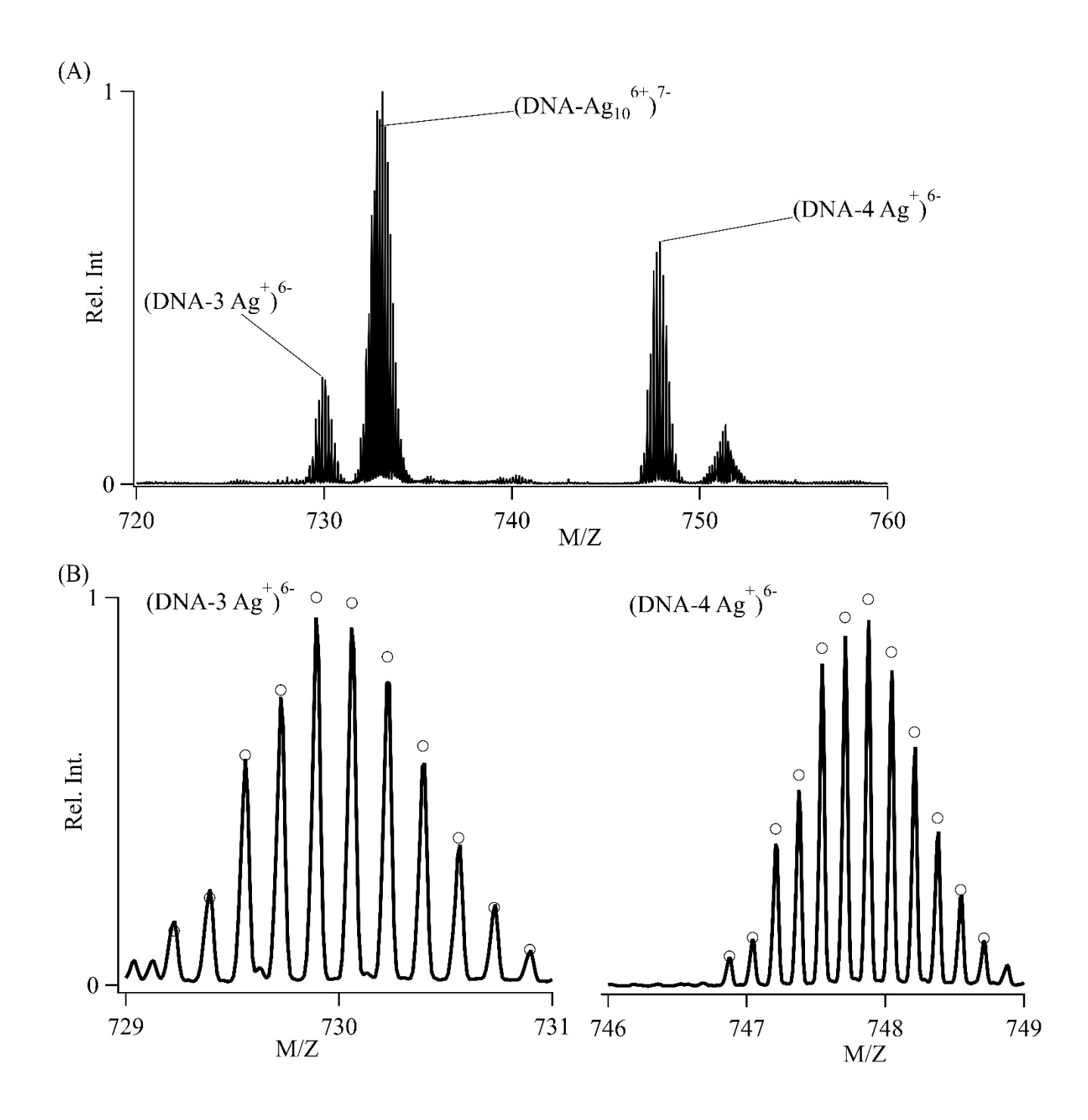
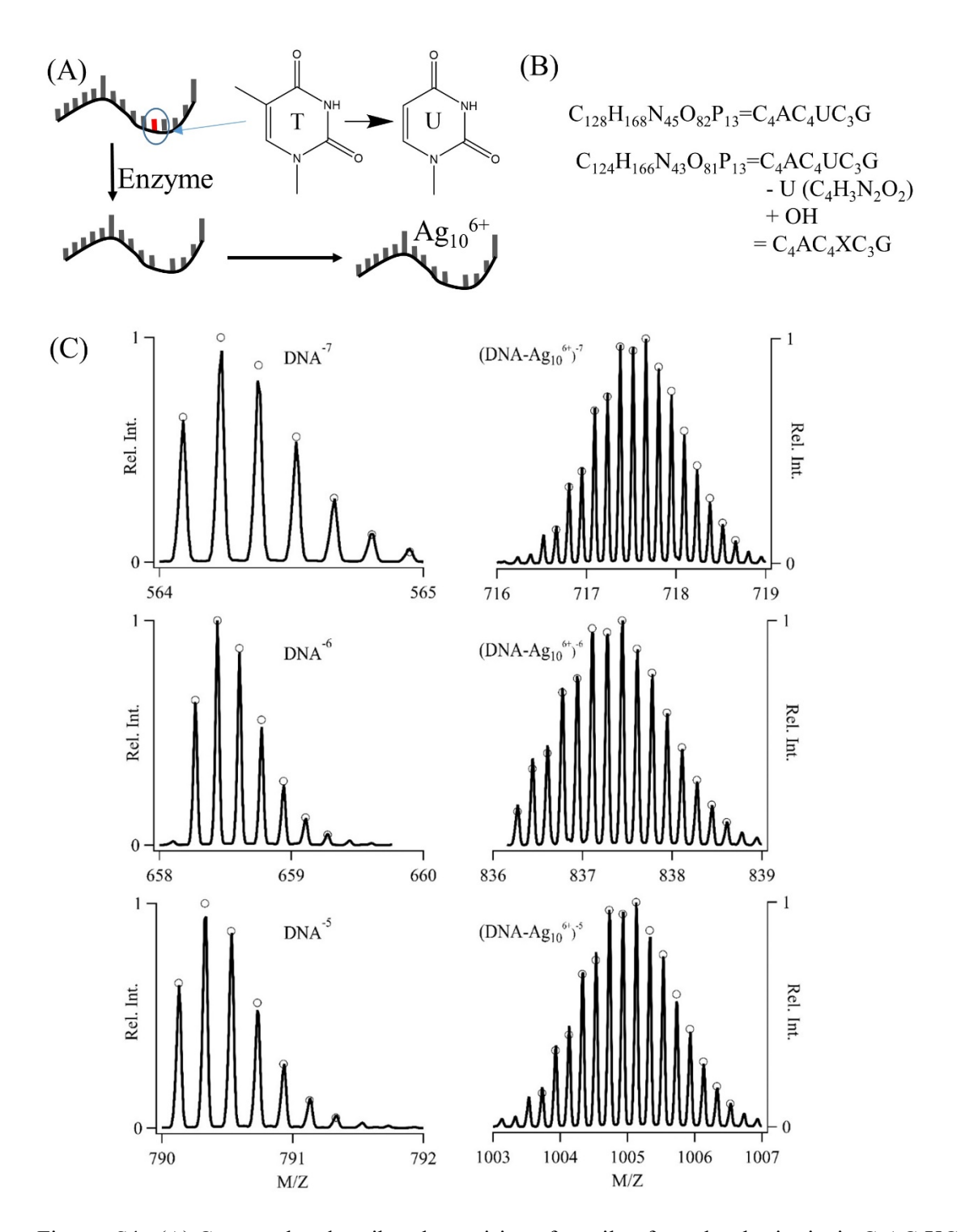


Figure S3: (A) A portion of the mass:charge spectrum of the C4AC4TC3G-Silver cluster sample. (B) Mass:charge spectrum of the -6 charge states of C4AC4TC3G with 3 and 4 Ag $^+$. The open circles predict the M/Z values for the -6 charged complexes with the formulas $C_{129}H_{\underline{167}}N_{45}O_{32}P_{13} + 3$ Ag $^+$ and $C_{129}H_{\underline{166}}N_{45}O_{32}P_{13} + 4$ Ag $^+$. The underlined hydrogens show that these oxidized Ag $^+$ adducts displace 3 and 4 phosphate-bound H $^+$.



Figures S4: (A) Cartoon that describes the excision of uracil to form the abasic site in $C_4AC_4XC_3G$. The thymine in $C_4AC_4TC_3G$ was first replaced with a uracil, which is then excised with Uracil DNA-Glycosylase. (B) Formulas for fully protonated $C_4AC_4UC_3G$ and $C_4AC_4XC_3G$. (C) Mass:charge spectrum of the -5, -6, and -7 charge states of $C_4AC_4XC_3G$ (left) and $C_4AC_4XC_3G$ -Ag₁₀⁶⁺ (right). The open circles predict the M/Z values based on the molecular formulas $C_{124}H_{\underline{161}}N_{43}O_{81}P_{13}^{5-}$, $C_{124}H_{\underline{153}}N_{43}O_{81}P_{13}Ag_{10}^{5-}$, $C_{124}H_{\underline{160}}N_{43}O_{81}P_{13}^{6-}$, $C_{124}H_{\underline{153}}N_{43}O_{81}P_{13}Ag_{10}^{7-}$, and $C_{124}H_{\underline{153}}N_{43}O_{81}P_{13}Ag_{10}^{7-}$.

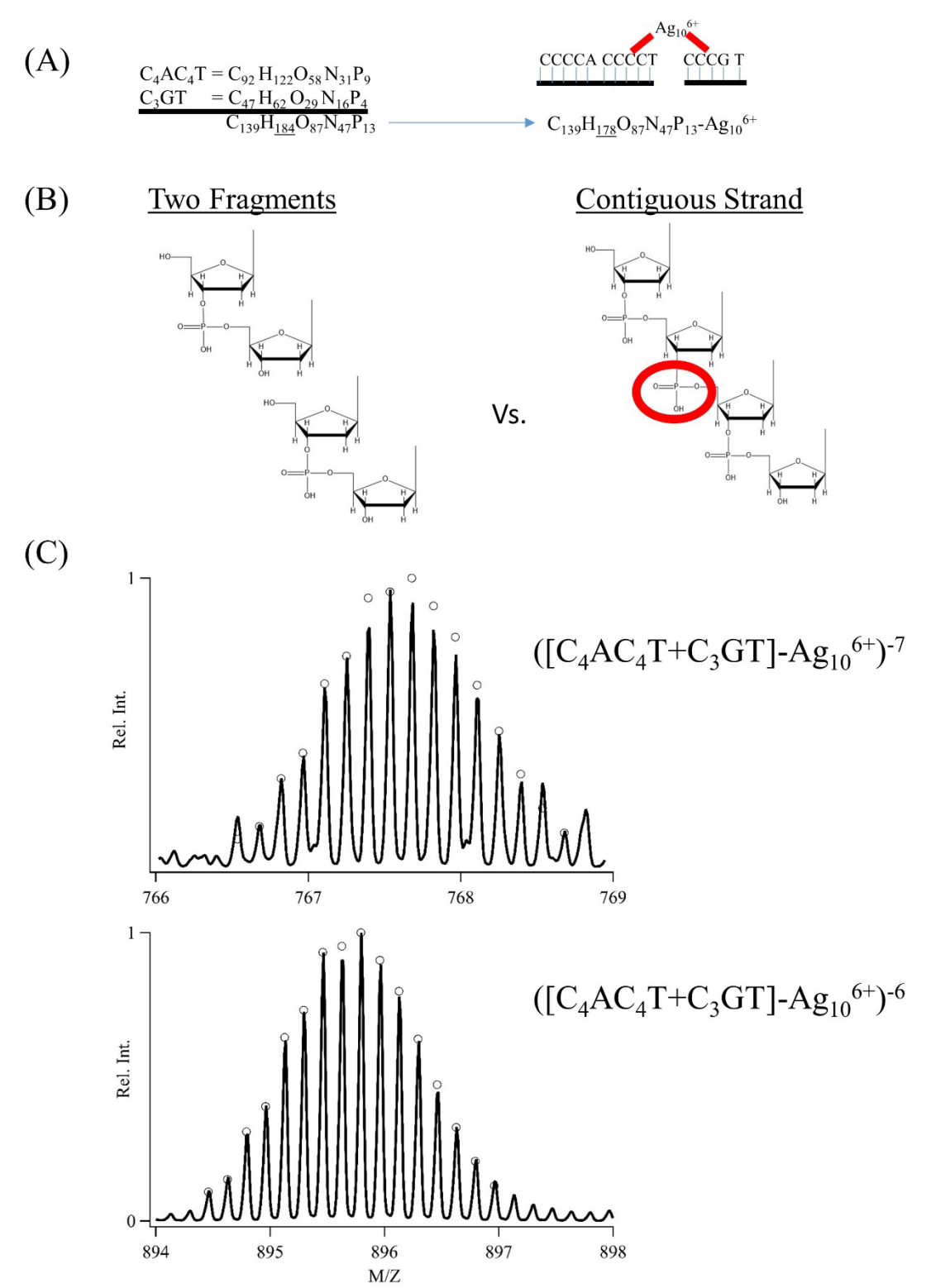


Figure S5: (A) Combined molecular formula of $C_4AC_4T + C_3GT$ with the linking Ag_{10}^{6+} cluster. (B) Structures show missing phosphate for the fragments in relation to the contiguous strand. (C) Mass:charge spectrum of the -7 and -6 charge states of $C_4AC_4T + C_3GT + Ag_{10}^{6+}$. The open circles predict the M/Z values based on the molecular formulas $C_{139}H_{165}N_{47}O_{87}P_{13}^{7-}$ and $C_{139}H_{166}N_{47}O_{87}P_{13}$ Ag_{10}^{6-} .

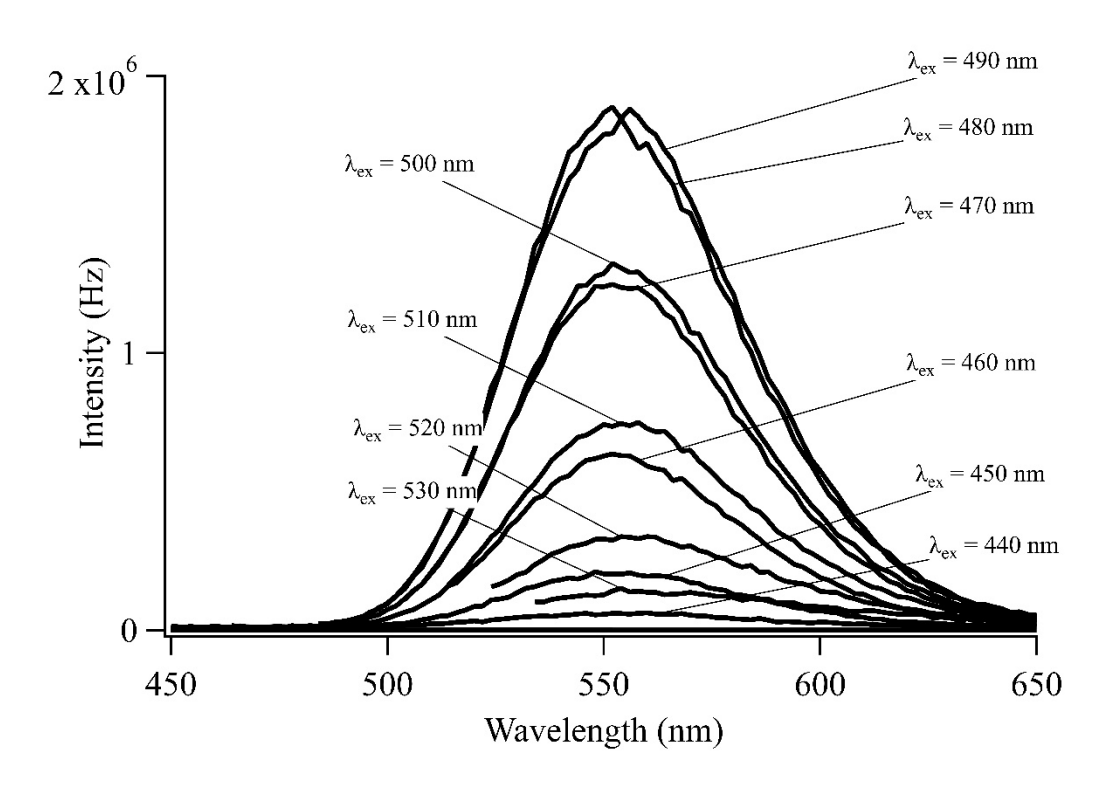


Figure S6: Emission spectra acquired with $\lambda_{ex} = 440 - 530$ nm. Consistent emission bands are consistent with Kasha's Rule and indicate that a single emissive species forms.

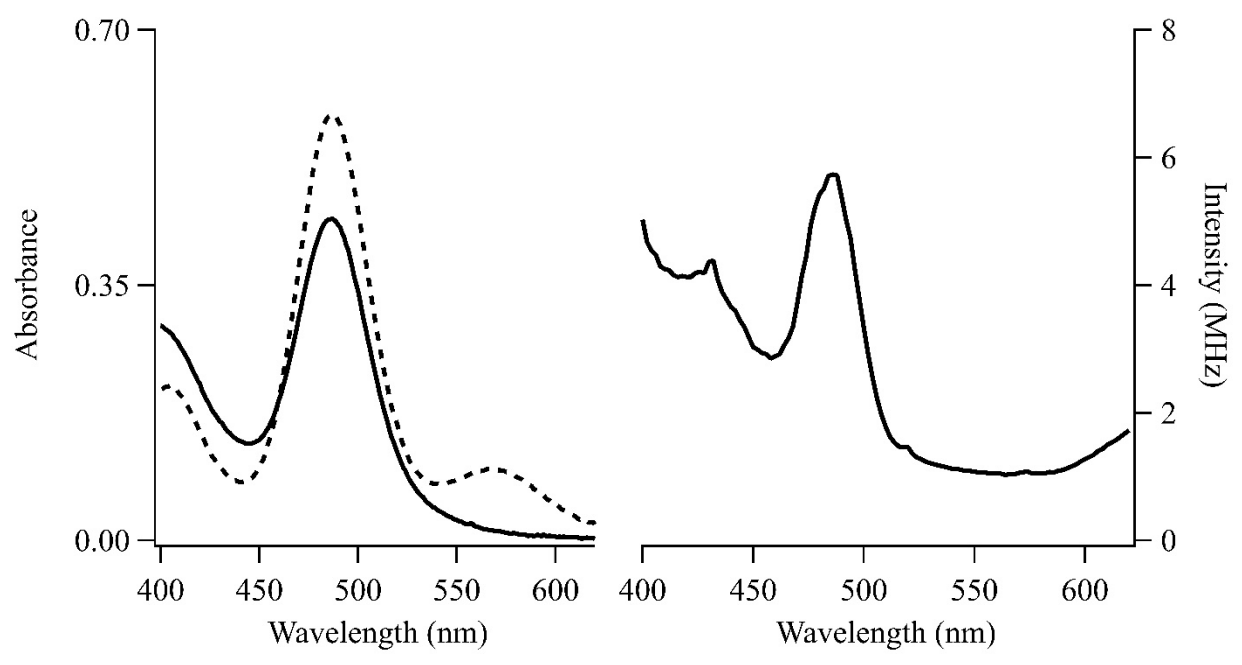


Figure S7: (Left) Absorption spectra at pH =7 (dotted) and pH = 10 (solid) both show strong absorption at 490 nm due to the Ag_{10}^{6+} cluster. However, the peak at ~570 nm is diminished at the higher pH, which suggests this is due to a chemically distinct cluster. (Right) Excitation spectrum in the cryogenic glass showing favored absorption at 490 nm.

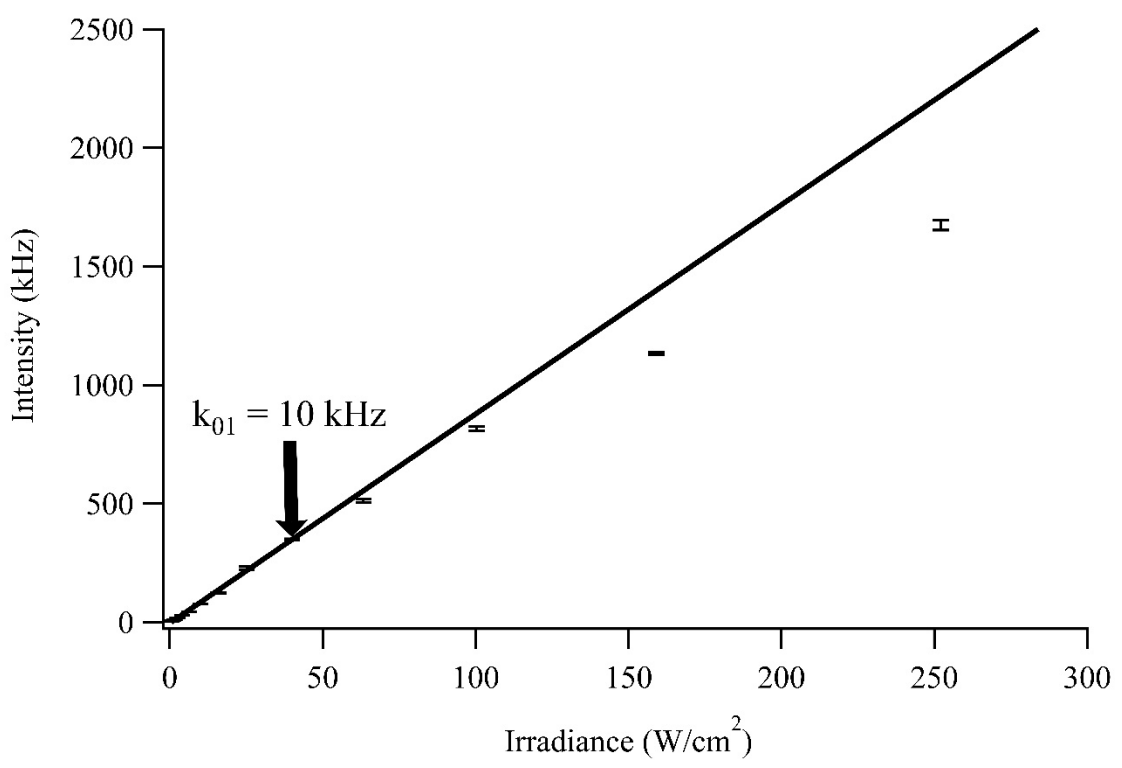


Fig. S8: Plot of fluorescence intensity vs. irradiance for $C_4AC_4TC_3G-Ag_{10}^{6+}$. The first 13 data points were used to create a linear fit, and subsequent measurements deviate from linearity at $\sim 50 \text{ W/cm}^2$.

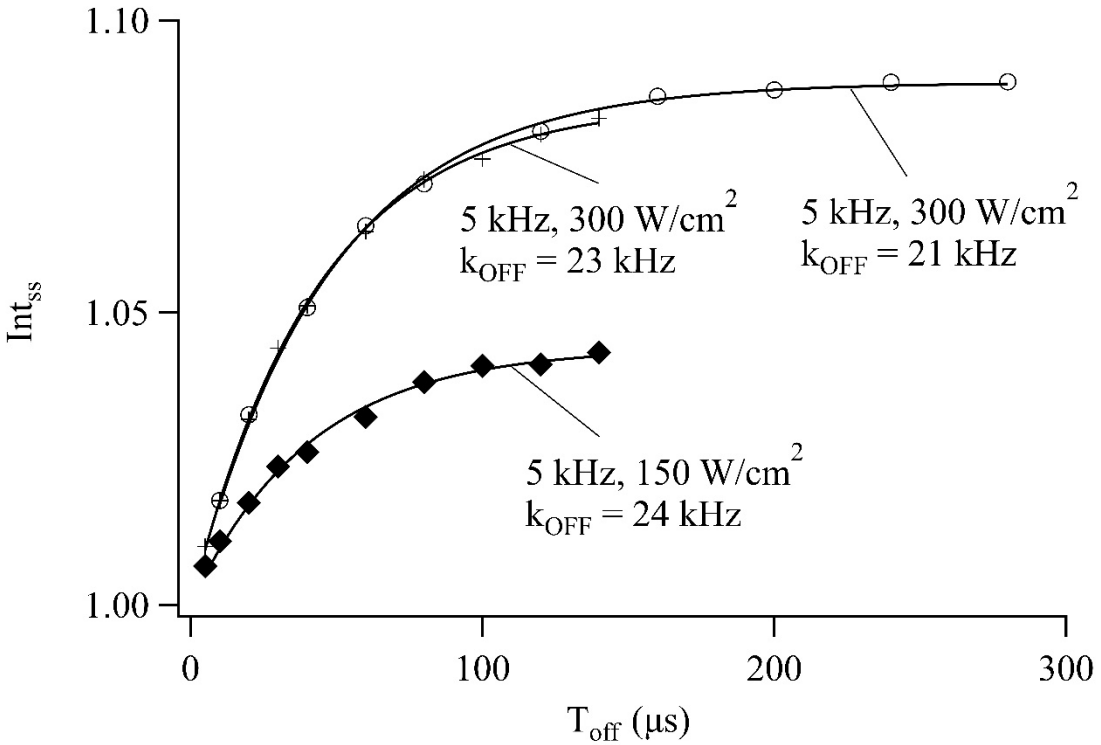


Fig. S9 Normalized intensities in the Bright State (Int_{SS}) as a function of the laser is off time (T_{OFF}). This data was fit using Equation 5 to determine k_{ON} and k_{OFF} . The laser was modulated at 5 (crosses) and 2.5 (open circles) kHz at 300 W/cm², and the laser intensity was reduced to 150 W/cm² at 5 kHz (closed diamond

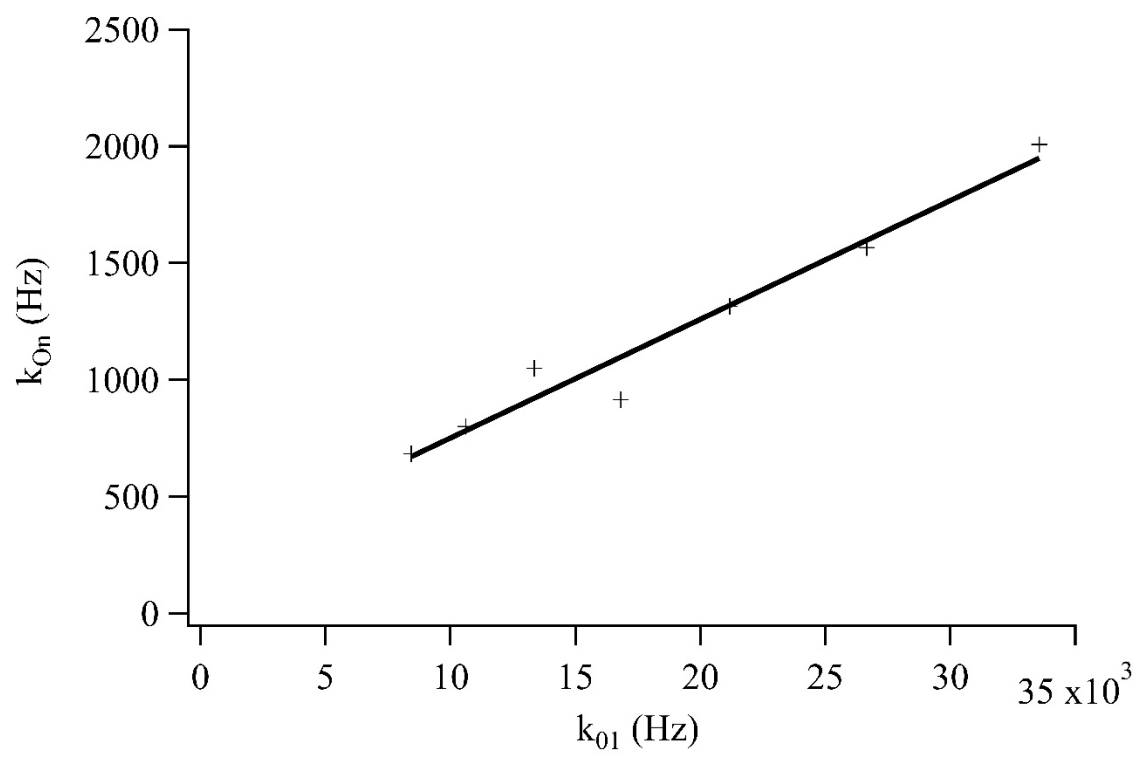


Figure S10: Dependence of k_{ON} with the excitation rate k_{01} . The data are fit with the equation $k_{ON} = k_{01} \phi_{12}$, where $k_{01} = \sigma I$ and I is the irradiance (W/cm²) and σ is the absorption cross-section (cm²).

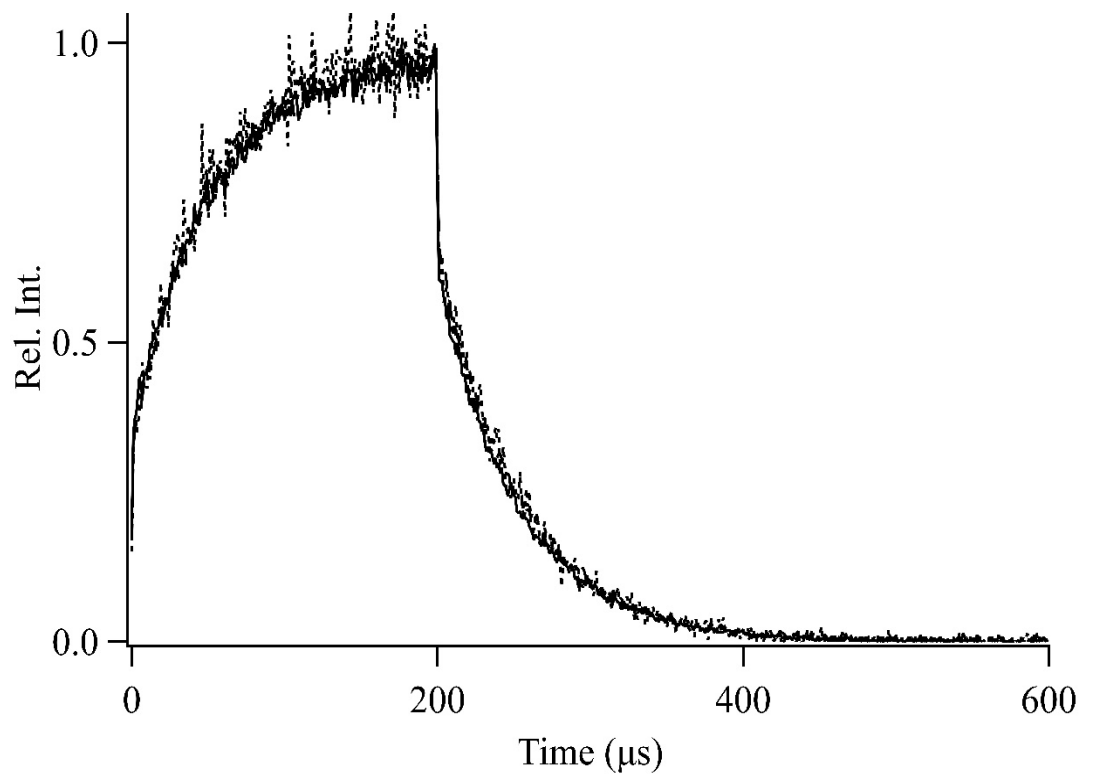


Figure S11: Time decay of the near-infrared luminescence using stock DNA solution (30 μ M, solid line), and a 5X (dotted line), and 20X (dashed line) diluted solutions. The similarities of the profiles suggests that the solutions are sufficiently dilute to avoid self-quenching.

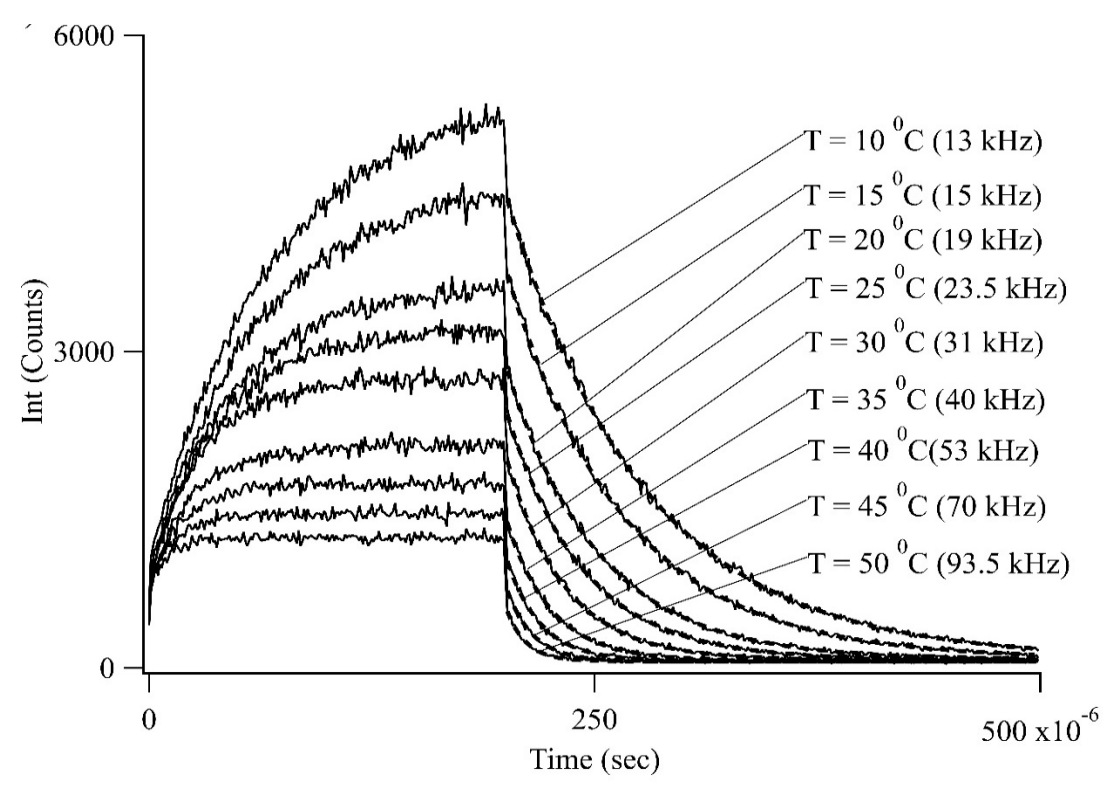


Figure S12: Time decays of the near-infrared luminescence as a function of temperature. The laser was modulated at 2 kHz wit T_{OFF} = 300 μs .

Table S1: Temperature Dependence of the off rates (koff) for the Three DNA Templates.

Temp (°C)	k _{OFF} (C ₄ AC ₄ TC ₃ G)	k _{OFF} (C ₄ AC ₄ XC ₃ G)	$k_{OFF}(C_4AC_4T + C_3GT)$
	(kHz)	(kHz)	(kHz)
11	12.9 ± 0.2	12.6 ± 0.4	24.7 ± 0.2
15	15.0 ± 0.4	14.9 ± 0.5	30.3 ± 0.2
20	19.2 ± 0.4	19.5 ± 0.6	37.2 ± 0.3
24	23.7 ± 0.2	23.8 ± 0.7	46.4 ± 1.6
29	31.0 ± 0.3	31.1 ± 0.8	57.8 ± 2.2
33	41.5 ± 1.7	41.4 ± 0.3	71.7 ± 3.5
38	55.7 ± 4.4	54.3 ± 2.0	76.9 ± 5.0
42	71.2 ± 2.6	74.7 ± 3.3	
47	99.9 ± 11.1	101.1 ± 9.8	

Appendix I:

The transitions in the Jablonski diagram (Fig. 2A) can be represented by a series of linear equations

$$\dot{X}(t) = M X(t)$$

where X(t) describes the state populations:

$$X(t) = \begin{bmatrix} S_0(t) \\ S_1(t) \\ S_2(t) \end{bmatrix}$$

and M is the rate constant matrix. With the laser on,

$$M_{on} = \begin{bmatrix} -k_{01} & k_{10} & -k_{12} \\ k_{01} & -k_{10} - k_{20} & 0 \\ 0 & -k_{20} & -k_{12} \end{bmatrix}$$

With the laser off,

$$M_{off} = \begin{bmatrix} 0 & k_{10} & -k_{12} \\ 0 & -k_{10} - k_{20} & 0 \\ 0 & -k_{20} & -k_{12} \end{bmatrix}$$

Diffusion is insignificant during the ~200 μ s time scale of our experiments because the DNA-silver complex complex diffuses slowly. This system of linear equations is solved by calculating the eigenvalues c_0 , c_1 , and c_2 and associated eigenvectors c_1 , c_2 , and c_3 are described by calculating the eigenvalues c_1 , and c_2 and associated eigenvectors c_1 , c_2 , and c_3 are described by calculating the

$$X(t) = b_0 P_0 e^{c_0 t} + b_1 P_1 e^{c_1 t} + b_2 P_2 e^{c_2 t}$$

where the constants b_i are determined by the intial conditions according to:

 $PB = X(t_0)$

and

$$B = \begin{bmatrix} b_0 \\ b_1 \\ b_2 \end{bmatrix}$$

$$P = \begin{bmatrix} P_0 & P_1 & P_2 \end{bmatrix}$$

The Mathematica Code that describes the time evolution between the states is provided below:

```
Clear["Global`*"]
TextCell["On Matrix"]
MOn=\{\{-k01, k10, kT\}, \{k01, -(kI+k10), 0\}, \{0, kI, -kT\}\};
MOn //MatrixForm
                            (*Check Rate Matrix*)
AOn=Eigenvalues[MOn]; (*Eigenvalues of On matrix*)
JOn=Eigenvectors[MOn];(*Eigenvectors of On matrix*)
HOn=LinearSolve[Transpose[JOn], {S0off,S1off,T1off}] (*Constants*);
QOn=HOn[[1]]*JOn[[1]] //FullSimplify; (*Vectors*)
ROn=HOn[[2]]*JOn[[2]] //FullSimplify;
TOn=HOn[[3]]*JOn[[3]] //FullSimplify;
TextCell["Off Matrix"]
MOff=\{\{0, k10, kT\}, \{0, -(kI+k10), 0\}, \{0, kI, -kT\}\};
MOff //MatrixForm
                               (*Check Rate Matrix*)
AOff=Eigenvalues[MOff]; (*Eigenvalues of matrix Off matrix*)
JOff=Eigenvectors [MOff]; (*Eigenvectors of matrix Off matrix*)
HOff=LinearSolve[Transpose[JOff], {$00n, $10n, $Tlon}] //FullSimplify; (*Constants*)
QOff=HOff[[1]]*JOff[[1]] //FullSimplify; (*Vectors*)
ROff=HOff[[2]]*JOff[[2]] //FullSimplify;
TOff=HOff[[3]]*JOff[[3]] //FullSimplify;
(*"General equation for Populations with Laser On"]*)
Son[S0off\_,S1off\_,T1off\_,t\_] = QOn*E^(AOn[[1]]*t) + ROn*E^(AOn[[2]]*t) + TOn*E^(AOn[[3]]*t);
(*General equation for Populations with Laser Off*)
Soff[S0on\_, S1on\_, T1on\_, t\_] = QOff*E^(AOff[[1]]*t) + ROff*E^(AOff[[2]]*t) + TOff*E^(AOff[[3]]*t);
(*Enter Constants*)
k01=60000; k10=800000000; kI=40000000; kT=20000;
(*Enter the Duty Cycle*)
cycle=0.6;
(*Enter the Period*)
tTOT=0.000200;
(*Enter the Time Steps and Number of Cycles*)
stepSize = 1*^-6;
numCycle = 4;
tON=cycle*tTOT;
                               (*Compute ON and OFF times*)
tOFF=(1-cycle)*tTOT;
c1=1; c2=0; c3=0; (*Initial Conditions*)
sumGS= \{c1\}; sumE = \{c2\}; sumD = \{c3\};
ttTOT = Table[i,{i,0, numCycle*tTOT, stepSize}]//N;
                                                          (*Setup time scale for all cycles*)
ttOn = Table[i, \{i, 0, tON, stepSize\}] /\!/ N \; ;
                                                              (*Setup time subwindows for individual on and off cycles*)
ttOff = Table[i, \{i, 0, tOFF, stepSize\}]//N;
(*For Loop for the multiple cycles*)
For[i=0,i<numCycle,i++,
 Son1=Son[c1,c2,c3,ttOn]; (*On populations in ground, emissive, and dark states.*)
 GSon = Drop[Son1[[1]],1]//N; (*Drop the first element in each list that is repeated from preceding cycle*)
 Eon = Drop[Son1[[2]],1]//N;
 Don = Drop[Son1[[3]],1]//N;
 c1 = Last[GSon] //N; (*Updated intial conditions*)
 c2 = Last[Eon]/N;
 c3 = Last[Don]//N;
 Soff1=Soff[c1,c2,c3,ttOff]; (*Off populations in ground, emissive, and dark states*)
 GSoff = Drop[Soff1[[1]],1]//N;
Eoff = Drop[Soff1[[2]],1]//N;
 Doff = Drop[Soff1[[3]],1]//N;
 c1 = Last[GSoff] //N ;(*Updated initial conditions*)
 c2 = Last[Eoff]//N;
 c3 = Last[Doff]//N;
 sumGS = Join[sumGS,GSon, GSoff]; (*Concatenate populuations in each state*)
 sumE = Join[sumE,Eon, Eoff];
 sumD = Join[sumD,Don, Doff];
sumGStime = Transpose[{ttTOT, sumGS}]; (*Setup (x,y) pairs*)
Export["a0.xls",sumGStime,"XLS"]; (*Export data*)
sumEtime = Transpose[{ttTOT, sumE}
Export["a1.xls",sumEtime,"XLS"];
sumDtime = Transpose[{ttTOT, sumD}];
Export["a2.xls",sumDtime,"XLS"];
```

Appendix II:

The following describes the analytical rate equations for our simplified model from Equation 1:

$$B \xrightarrow{k_{ON}} D$$
Eq. 1

When the laser is on from 0 to t_{ON}, the following rate equations results when using mass balance:

$$\frac{dB_{ON}}{dt} = -k_{ON}B_{ON} + k_{OFF}L_2 = -(k_{ON} + k_{OFF})B_{ON} + k_{OFF}$$

$$\frac{dD_{ON}}{dt} = +k_{ON}B_{ON} - k_{OFF}D_{ON} = -(k_{ON} + k_{OFF})D_{ON} + k_{ON}$$

Integrating from 0 to toN gives:

$$B_{ON}(t) = \frac{k_{OFF}}{k_{ON} + k_{OFF}} + \frac{k_{ON}}{k_{ON} + k_{OFF}} e^{-(k_{ON} + k_{OFF})t_{ON}}$$
Eq. 2
$$D_{ON}(t) = \frac{k_{ON}}{k_{ON} + k_{OFF}} \left(1 - e^{-(k_{ON} + k_{OFF})t_{ON}}\right)$$

In the limit of $t_{ON} = 0$, $B_{ON} = 1$ and $D_{ON} = 0$, consistent with no crossing to from B to D.

In the limit of $t_{ON} = \infty$, steady state populations are reached:

$$B_{ON,SS} = \frac{k_{OFF}}{k_{ON} + k_{OFF}}$$
 Eq. 3
$$D_{ON,SS} = \frac{k_{ON}}{k_{ON} + k_{OFF}}$$

Thus, the two steady-state state populations satisfy mass balance between the two states.

When the laser is off, $k_{ON} = 0$ and the rate equations simplify:

$$\frac{dB}{dt} = k_{OFF}D = k_{OFF}(1 - B)$$

$$\frac{dD}{dt} = -k_{OFF}D$$

Integrating from 0 to T_{OFF} and from the starting steady state populations:

$$B_{OFF}(t) = 1 - \frac{k_{ON}}{k_{ON} + k_{OFF}} e^{-k_{OFF}T_{OFF}}$$
 Eq. 4

$$D_{OFF}(t) = \frac{k_{ON}}{k_{ON} + k_{OFF}} e^{-k_{OFF}T_{OFF}}$$
 Eq. 6

In the limit of $T_{OFF} = 0$,

$$B_{OFF}(t) = 1 - \frac{k_{ON}}{k_{ON} + k_{OFF}} = \frac{k_{OFF}}{k_{ON} + k_{OFF}}$$

$$D_{OFF}(t) = \frac{k_{ON}}{k_{ON} + k_{OFF}}$$

which matches the steady-state values.

In the limit of $t = \infty$,

$$B_{OFF}(t) = 1$$

$$D_{OFF}(t) = 0$$

which is consistent with a fully relaxed D state.

The fluorescence decay was analyzed using

$$Int_{SS} = \frac{B_{OFF}(t)}{B_{ON,SS}} = \frac{1 - \frac{k_{ON}}{k_{ON} + k_{OFF}} e^{-k_{OFF}T_{OFF}}}{\frac{k_{OFF}}{k_{ON} + k_{OFF}}} = 1 + \frac{k_{ON}}{k_{OFF}} \left(1 - e^{-k_{OFF}T_{OFF}}\right)$$
 Eq. 5